PRIMA mission concept

Glenn, Jason; Meixner, Margaret; Bradford, Charles M.; Pontoppidan, Klaus; Pope, Alexandra; Kataria, Tiffany; Rocca, Jennifer; Luthman, Elizabeth; Baselmans, Jochem; More Authors

DOI
10.1117/1.JATIS.11.3.031628

Publication date
2025

Document Version
Final published version

Published in
Journal of Astronomical Telescopes, Instruments, and Systems

JATIS Journal of Astronomical Telescopes, Instruments, and Systems

RESEARCH PAPER

PRIMA mission concept

Jason Glenn,[a,*] Margaret Meixner,[b] Charles M. Bradford,[b] Klaus Pontoppidan,[b] Alexandra Pope,[c] Tiffany Kataria,[b] Jennifer Rocca,[b] Elizabeth Luthman,[b] Lee Armus,[d] Jochem Baselmans,[e,f] Cara Battersby,[g] Alberto Bollato,[h] Denis Burgarella,[i] Weibo Chen,[b] Laure Ciesla,[i] Peter Day,[b] Anna Di Giorgio,[j] Michael Dipirro,[a] Charles Darren Dowell,[b] Pierre Echternach,[b] Thomas Essinger-Hileman,[a] Marc Foote,[b] Carlotta Gruppioni,[j] Brandon Hensley,[b] Thomas Henning,[k] Willem Jellema,[l] Matthew Johnson,[b] Alan Kogut,[a] Oliver Krause,[k] James McGuire,[b] Elisabeth Mills,[m] Arielle Moullet,[n] Michael Rodgers,[b] Marc Sauvage,[o] John D. Smith,[p] Rachel Somerville,[q] Johannes Staguhn,[a] Thomas Stevenson,[a] Carole Tucker,[r] Stephen Unwin,[b] John Ziemer,[b] Matthew Cannella,[s] and Richard Dissly[s]

[a]Goddard Space Flight Center, Greenbelt, Maryland, United States
[b]California Institute of Technology, Jet Propulsion Laboratory, Pasadena, California, United States
[c]University of Massachusetts, Department of Astronomy, Amherst, Massachusetts, United States
[d]Caltech, Infrared Processing and Analysis Center, Pasadena, California, United States
[e]TU Delft, Faculty of EEMCS, Delft, The Netherlands
[f]SRON Leiden, Leiden, The Netherlands
[g]University of Connecticut, Department of Physics, Storrs, Connecticut, United States
[h]University of Maryland, Department of Astronomy, College Park, Maryland, United States
[i]Aix Marseille Univ, CNRS, CNES, Laboratoire d'Astrophysique de Marseille, Marseille Cedex 13, France
[j]Istituto Nazionale di Astrofisica: Osservatorio di Astrofisica e Scienza dello Spazio di Bologna, Bologna, Italy
[k]Max Planck Institute for Astronomy (MPIA), Heidelberg, Germany
[l]SRON Groningen, Groningen, The Netherlands
[m]University of Kansas, Department of Physics and Astronomy, Lawrence, Kansas, United States
[n]National Radio Astronomy Observatory (NRAO), Charlottesville, Virginia, United States
[o]Université Paris-Saclay, Univ. Paris Cité, CEA, CNRS, AIM, Gif-sur-Yvette, France
[p]The University of Toledo, Department of Physics and Astronomy, Toledo, Ohio, United States
[q]Flatiron Institute, Center for Computational Astrophysics, New York, United States
[r]Cardiff University, School of Physics and Astronomy, Cardiff, United Kingdom
[s]BAE Systems, Inc., Space & Mission Systems, Boulder, Colorado, United States

ABSTRACT. The Astro2020 Decadal Survey recommended a new line of astrophysics observatories intermediate in scale between MIDEXs and Flagship-class observatories. In response, NASA created the Astrophysics Probe Explorer class and solicited proposals for the first generation of Probes. With a larger cost cap, Probes can achieve more ambitious science than SMEXs or MIDEXs and be implemented faster than Flagships—as frequently as one per decade. The PRobe far-Infrared Mission for Astrophysics (PRIMA) is one of two Probe concepts selected by NASA for a concept study in 2024/2025, potentially leading to implementation and launch as early as 2031. PRIMA was designed for a broad range of astrophysics, from how planets assemble their atmospheres, to the coevolution of galaxies and black holes, to the evolving properties of dust and galactic metallicity over cosmic time. Seventy-five percent of PRIMA's observing time will be allocated to guest observer observations and 25% allocated to principal investigator science; however, the principal investigator science data will be available promptly for guest investigator usage. The observatory features a 1.8-m diameter telescope cooled to 4.5 K with two science instruments: the Far-InfraRed Enhanced Survey Spectrometer (FIRESS) and the

*Address all correspondence to Jason Glenn, jason.glenn@nasa.gov

PRIMA imager (PRIMAger). FIRESS provides continuous spectral coverage from 24 to 235 μm, in two spectral resolution modes ($R \geq 85$ and $R = 4400(112\ \mu\text{m}/\lambda)$), with spectral mapping capability and order-of-magnitude sensitivity improvement over previous observatories. PRIMAger delivers similar sensitivity advances and first-of-its-kind far-infrared hyperspectral imaging for astrophysics with $R \sim 8$ from 25 to 84 μm, and polarimetry in four broadband filters from 80 to 261 μm. PRIMA's science and technical motivation is outlined, its overall architecture is described, and its cryogenic payload and instruments, including the kinetic inductance detector arrays, and operations and observing modes, are summarized.

Keywords: far infrared; kinetic inductance detectors; telescopes; galaxies; protoplanetary disks

Paper 25028SS received Jan. 31, 2025; revised May 15, 2025; accepted Jun. 11, 2025; published Jul. 29, 2025.

1 Introduction: PRIMA and a New Class of NASA Astrophysics Missions

In *Pathways to Discovery in Astronomy and Astrophysics for the 2020s*[1] (hereinafter Astro2020), the Astronomical Decadal Survey recommended a new class of space observatories: astrophysics Probes. The scale of the Probes fills the gap between MIDEXs on the smaller side (e.g., SPHEREx for a recent example[2]) and Flagship Missions (e.g., JWST[3] and HWO[4]). NASA responded with a call for concept proposals for X-ray and far-infrared (far-IR) Probes that were due in November 2023. With a $1.5 billion cost cap, Probes can accomplish more ambitious science than MIDEXs and launch more frequently than Flagship missions—perhaps one per decade. This higher cadence than Flagships (which have 2+ decade development and implementation phases) and intermediate scale enables NASA both to take advantage of maturing technologies and to have Explorer-like principal investigator (PI) science and community-driven general observer (GO) and guest investigator (GI) science programs. Indeed, the APEX Announcement of Opportunity mandated that at least 70% of observing time be reserved for GO science and that all PI science data be made available rapidly for GI science. The PI-managed cost cap for Probes is $1.0 billion, with $500 million reserved for the launch vehicle and services (~$150 million) and administration (by NASA) of competed GO and GI science (~$350 million).

The PRobe far-Infrared Mission for Astrophysics, or PRIMA, was selected for a phase A study in late 2024, which will be due in late 2025. PRIMA will have an actively cooled 1.8-m primary mirror and two instruments sensitive to wavelengths between 24 and 261 μm: FIRESS, a dispersive spectrometer with a Fourier Transform Module (FTM) for increased spectral resolving power, and PRIMAger, a hyperspectral imager and polarimeter (Table 1). Both instruments will use arrays of superconducting kinetic inductance detectors (KIDs), totaling ~12,000 pixels. The combination of extreme KID sensitivity achieved in recent years and the 4.5 K telescope enable sensitivities limited or very nearly limited by astrophysical photon noise—from the zodial light at short wavelengths and Galactic dust emission at longer wavelengths. The spectral coverage nearly bridges the greater than 10× gap between *JWST* and ALMA, *where there is currently no astronomical observational capability*, and the 1.8-m aperture and newly achieved detector performance enable vastly more sensitive observations than could be achieved with warmer telescopes and detectors with intrinsically higher noise. Thus, PRIMA builds on the scientific legacies of *IRAS*,[5] *ISO*,[6] *Spitzer*,[7] *AKARI*,[8] *Herschel*,[9] and the Stratospheric Observatory for Infrared Astronomy (*SOFIA*)[10] as well as the science cases and technology development for prior far-IR concepts, such as SPICA,[11] GEP,[12] and Origins Space Telescope.[13,14]

PRIMA is designed to address the three science goals listed in Astro2020 for a far-IR Probe: tracing the astrochemical signatures of planet formation, measuring the formation and buildup of galaxies, heavy elements, and dust, and probing the coevolution of galaxies and their supermassive black holes across cosmic time. This paper summarizes the PRIMA PI science case and the current state of the observatory architecture, instrumentation, detectors, and observing modes, which are designed to realize the science goals. PRIMA's two instruments and their science

Table 1 PRIMA concept parameters.

Telescope	1.8-m diameter primary mirror, all aluminum, 4.5 K
FIRESS	24 – 235 μm
Low resolution	$R > 85$ mapping and pointed spectroscopy
High resolution	$R \sim 4400 \times (112\ \mu\text{m}/\lambda)$ spectroscopy
PRIMAger	24 to 261 μm
Hyperspectral imaging (PHI)	$R \sim 8$ at 25 to 84 μm
Polarimetric imaging	$R \sim 4$ at 91, 125, 165, & 232 μm
Detectors	0.1 K kinetic inductance detectors (KIDs)
	FIRESS 8064 KIDs total, PRIMAger 3951 KIDs total
Orbit	Sun-Earth L2
Launch	2031
Minimum operational lifetime	5 years
Observing time	25% principal investigator
	75% general observer

drivers are described in detail in companion papers on the Far-Infrared Enhanced Survey Spectrometer (FIRESS, see Bradford et al., and Pontoppidant et al., this volume) and the PRIMA Imager (see Ciesla et al., and Burgarella et al., this volume). Seventy-five percent of PRIMA's observing time will be allocated to GO science, with GO observations beginning shortly after commissioning. PRIMA anticipates a launch in 2031 and a minimum 5-year lifetime in a halo orbit around the Sun-Earth Lagrange point (L2), selected for its stable thermal environment and relatively large downlink bandwidth. The instantaneous field of regard of approximately one-quarter of the sky (limited by Sun and Earth avoidance to prevent payload heating) sweeps through the entire sky with a period of 6 months. With no consumables beyond propellant, its potential lifetime is ~10 years.

2 PRIMA Science: Vast New Potential Enabled by Concerted Technology Development

2.1 New Era of KID-Enabled Far-IR Science

PRIMA greatly increases the reach of far-IR science enabled by the sensitivity and versatility of KIDs. Because of the range of architectures possible with microresonators, KIDs have shown surprising promise and adaptability, with applications ranging from X-ray to millimeter wavelengths since their inception in 2003.[15] Over the past decade, there have been concerted efforts both in the U.S.[16,17] and Europe[18] to develop far-IR KIDs to enable new far-IR astronomy with superb sensitivity, large arrays, and robustness to cosmic rays. KIDs have not been deployed in space observatories yet; however, several ground-based instruments with KID focal planes have yielded astronomical observations and results.[19–23]

At 24 to 84 μm, PRIMAger couples KID arrays with linearly variable filters to provide fast hyperspectral mapping, yielding spectral data cubes over large solid angles. At longer wavelengths (84 to 261 μm), antenna-coupled, polarization-sensitive KIDs with linearly clocked antenna orientations enable polarimetric imaging (Dowell et al., this volume). The $1/f$ noise is mitigated by combining PRIMA's cold, ultrastable thermal platform (all optics $\leq$4.5 K) with modulation by scan mapping and rapid beam steering, avoiding the need for a polarization modulator. However, owing to near background-limited photon (BLIP) sensitivity, PRIMA's greatest leap in capability is in low- ($R \sim 100$) and moderate-resolving power spectroscopy ($R \lesssim 20{,}000$). FIRESS' dispersive spectroscopy matches the astrophysical backgrounds to the intrinsic detector

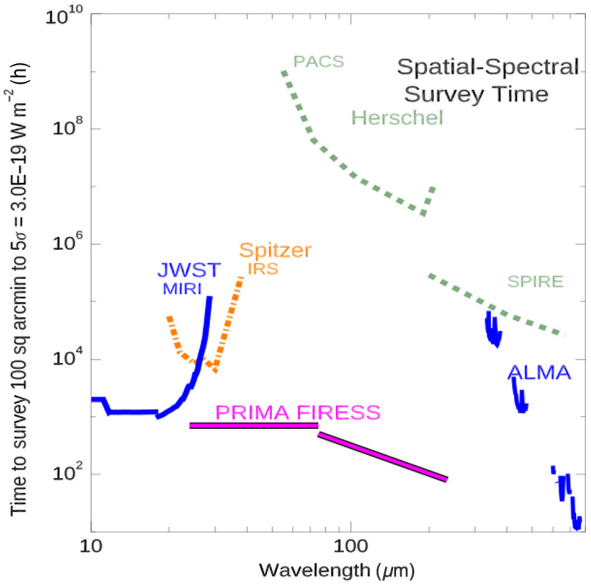

Fig. 1 Observing time to survey 100 square arcmin of sky with PRIMA FIRESS (in its non-Fourier Transform mode) as a function of wavelength. Solid magenta lines correspond to the sensitivity requirements (see Bradford et al. this issue for current best estimates of sensitivity). The blue solid (short wavelengths), orange dot-dash, green-dotted, and blue solid (long wavelengths) represent the spectral mapping speeds of *JWST-MIRI*, *Spitzer-IRS*, *Herschel*, and *ALMA*, respectively. This plot refers to measurement of integrated (unresolved) line fluxes in unresolved point sources in a map. The linewidth for the purposes of ALMA sensitivity are assumed to be 300 km/s ($R = 1000$). We note that JWST MIRI time is dominated by overheads for this 100 square arcmin fiducial observation.

noise and its long slits enable spectral mapping with sensitivity vastly exceeding previous observatories, bridging the spectral gap between JWST and ALMA (Fig. 1).

The PI-led surveys are described briefly below and in more detail in Pontoppidan et al. and Burgarella et al. (this volume). The PI observations become public as soon as they are processed to level 3 (basic calibrated data products) by the PRIMA science data pipeline and therefore comprise a powerful legacy for GI science while also demonstrating the capability of PRIMA for GO science. We anticipate this to be within 4 weeks after data acquisition for initial calibration and with improved reprocessing as better calibrations become available. PI observations will be distributed over the first 3 years, enabling GO observations to begin early in the mission lifetime to provide maximum benefit to the community.

Motivated by PRIMA's potential, we invited members of the scientific community to contribute science use cases to a GO science book. The response was vigorous, with 76 contributions,[24] ranging from Solar System science to cosmology and an all-sky survey. Although GO programs will be selected via a competitive process, the GO book represents a total of 80% of the expected GO observing time in the nominal 5-year mission lifetime. The use cases addressed more than 70% of the science questions identified in Astro2020, indicative of the scientific reach of unprecedented far-IR observations of the type enabled by PRIMA.

2.2 Origins of Planetary Atmospheres

The origins of exoplanetary systems, and their likelihood to form planets and moons with abundant elements necessary to be hospitable to life, are largely determined by processes happening during their first few million years, whereas protoplanetary disks retain enough gas to form giant planets.[25,26] Planet formation processes remain shrouded in mystery because current techniques cannot reliably measure the fundamental properties of a protoplanetary disk throughout the relevant planet-forming region, including its water and total gas mass. PRIMA is designed to determine the distribution of the water reservoir in a large sample of protoplanetary disks by measuring a large number of water lines tracing gas at all temperatures and the total mass of planet-forming gas as a function of stellar mass and evolutionary stage using the ground-state

line of HD at 112 μm. This will address long-standing questions on the importance of water in the formation of planetesimals[27,28] and giant planet cores,[29] the carbon-to-oxygen ratio of gas forming giant planet atmospheres,[30,31] the efficiency of volatile transport in planet-forming regions,[32–34] and the time scale for disk dissipation.[35–37] Only the far-IR has access to accurate tracers of cool water and H_2 and is therefore essential for providing a complete picture of the formation of exoplanets. These measurements will be made using FIRESS FTM observations of 200 protoplanetary disks. More than 200 potential protoplanetary disks with appropriate parameters ($0.5\,M_\odot > M_* > 1.5\,M_\odot$, ages of 1 to 10 Myr, within ~200 pc) have already been observed with JWST MIRI[38] and ALMA (e.g., Refs. 39 and 40) and are excellent candidates for the PRIMA target list. The final list will be defined based on our state of knowledge closer to launch.

2.3 Evolution of Galactic Ecosystems

In the local Universe, every massive galaxy hosts a supermassive black hole (SMBH) in its center, and the SMBH mass and galaxy stellar mass are strongly correlated.[41] SMBHs grow by accreting gas from the central regions of galaxies, whereas galaxies' stellar masses grow over vastly larger scales, fed by gas inflowing from the cosmic web.[42,43] It is not clear how this fundamental correlation was established: Did the SMBHs and stellar mass grow in lockstep or along different pathways? Are galactic outflows the key link that couples them?

Cosmic integrated black-hole accretion and star formation have evolved in unison since cosmic noon.[44] Studies based on soft X-ray to near-IR observations at $z \sim 1$ to 2 are severely limited by obscuration from thick columns of gas and dust,[45] and measure black hole accretion rates (BHARs) and star-formation rates (SFRs) in different galaxy populations. Only far-IR (25 to 300 μm) observations can measure both BHAR and SFR in highly obscured regions of the same galaxies. PRIMA's survey speed enables simultaneous BHAR and SFR measurements in large ($N > 150{,}000$) samples of galaxies at $z \sim 0.5$ to 2.5 to distinguish between models and to establish how the growth of SMBHs couples with the evolution of their host galaxies.

Winds ejected from active black holes into the circumgalactic medium and containing large masses of gas are a key feedback mechanism linking SMBHs and galaxy growth. Models invoke these winds to quench star formation in massive galaxies because they provide a mechanism to both remove star-forming gas and to prevent new gas from accreting.[46] These models are largely unconstrained given the lack of measured wind properties, such as their velocities and mass outflow rates.[47] Measurements of the cool (molecular and neutral atomic, $T < 10^4$ K) wind component, which dominates the outflowing mass, are limited to small samples (<20) of local galaxies.[48] In addition to the SFR and the BHAR, PRIMA can link these processes by measuring the mass outflow rates of cool galactic winds in active galaxies out to $z \sim 2$.

2.4 Buildup of Dust and Metals

Because the first massive stars began exploding as supernovae after cosmic dawn, the Universe has produced a growing complement of heavy elements (metals) that play fundamental roles in the formation of galaxies, stars, and planetary systems. When metals are injected into the interstellar medium (ISM) by asymptotic giant branch (AGB) stars and supernovae,[49] a large fraction is converted to dust—a near-universal step in their complex journey to forming planetary systems, including our own solar nebula.[50] The remarkably efficient growth and evolution of dust from metals over cosmic time remains a mystery.[51]

PRIMA provides key far-IR tracers of dust and metals at two pivotal times in the Universe: spectroscopy at cosmic noon (i.e., the peak of metal and dust production) and imaging polarimetry of the present-day ($z = 0$) Universe. These data directly address two unsolved, yet crucial, questions about the co-evolution of dust and metals. First, how has the relationship between gas-phase heavy-element contents (metallicity) and the mass fraction of small-grain dust traced with polycyclic aromatic hydrocarbons (PAHs) in galaxies changed since cosmic noon ($z \simeq 2$)? PRIMA measures the PAH-metallicity relationship at cosmic noon because PAH bands have redshifted into the far-IR. Second, what are the relative contributions of dust formed in the expanding envelopes of dying stars (stardust) versus dust formed in the ISM? PRIMA teases these contributions apart by measuring the polarization of far-IR emission from dust in local galaxies. These measurements are enabled with spectroscopic surveys of 100 galaxies and

polarimetric mapping of 30 local galaxies, respectively. Although final target lists may be revised based on improvements in the field before launch, a potential reference mission target list has already been assembled.

As described in Burgarella et al. (this volume), the *Evolution of Galactic Ecosystems* and *Buildup of Dust and Metals* science cases use imaging surveys with PRIMAger. PRIMA, similar to all single-aperture far-infrared telescopes, must cope with extragalactic source confusion caused by background galaxies. However, PRIMAger has a strong advantage in that it can use its own short wavelength (25 μm) positional priors with 4-arcsecond pixels and densely sampled spectral energy distributions for source deblending at longer wavelengths. This overcomes concerns about far-infrared emission arising from galaxies different from positional priors based on, e.g., optical-wavelength observations. PRIMA's confusion is assessed in Ref. 52 and the use of hyperspectral imaging for overcoming confusion is described in Ref. 53.

3 Concept Architecture

PRIMA combines a 1.8-m telescope with spectroscopic (Bradford et al., this volume) and imaging (Ciesla et al., this volume) instruments using the most sensitive far-IR detectors (KIDs) ever flown (Fig. 2). The telescope is conservatively designed using all aluminum material and proven manufacturing techniques that will be demonstrated early in the project activities, prior to the preliminary design review. A primary mirror diameter of 1.8 m is chosen to deliver the required sensitivity, with sufficient angular resolution to meet the primary science objectives within the cost cap for the Astrophysics Probe line. To approach the astrophysical background sensitivity limit, PRIMA's design minimizes emission from the telescope, relay optics, and structures by cooling them to $\leq$4.5 K. 4.5 K is sufficiently cold to eliminate self-emission from all but the longest-wavelength channels of the spectrometer and the longest-wavelength band of the imager and is straightforward to achieve with high-heritage approaches. PRIMA uses passive stages along with active cooling at 18 K and 4.5 K provided by the JWST flight-spare

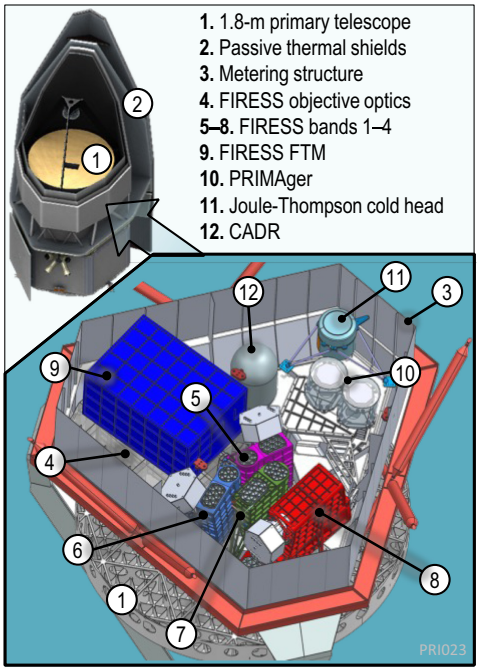

Fig. 2 Two views of the PRIMA spacecraft: The upper left shows the observatory looking down on the 1.8-m primary mirror (labeled item number 1) with the radiation shields (item 2) behind it and the warm spacecraft bus below it. The expanded lower-right panel shows the cryogenic payload mounted to the metering structure (item 3) behind the primary mirror. The telescope will be 4.5 K and the instrument optics 1 K (items 4 to 10), with the focal planes at 100 mK. Telescope and optics cooling are provided by the Joule-Thompson cold head (item 11) and pulse-tube cooler and 100 mK by the continuous adiabatic demagnetization refrigerator (item 12).

cryocooler,[54] with ^{3}He replacing ^{4}He as the working fluid. A continuous adiabatic demagnetization refrigerator (CADR) cools the instrument optics to 1 K and focal planes to 0.1 K. Stray light is controlled with careful use of baffles and by blackening the secondary support struts; as with JWST and Herschel, a full barrel around the telescope is not required.

The FIRESS instrument deploys four spectral bands, with similar designs for simplicity, which provide low- ($R \geq 85$) and high-resolution ($R \sim 4400 \times 112$ μm/λ) spectroscopy across the full 24 to 235 μm range, as required by the buildup of dust and metals and origins of planetary atmospheres science themes, respectively. The PRIMAger instrument has two parallel channels: hyperspectral imaging and broad-band polarimetric imaging. The hyperspectral channel provides $R \sim 8$ spectral imaging from 24 to 84 μm required by the extragalactic surveys that support the galactic ecosystems and buildup of dust and metal themes. FIRESS has greater spectral coverage and higher spectral resolution than PRIMAger's hyperspectral imager, but the hyperspectral imager has greater mapping speed. The four broad ($R \sim 4$) polarization bands at ~91, 125, 165, and 232 μm are required by the extragalactic surveys to cover the whole spectral energy distributions, and the polarization capability is driven by local galaxy imaging that supports the buildup of dust and metals theme.

PRIMA's KIDs, employed by both FIRESS and PRIMAger, leverage significant technology development and offer ~10× more pixels and 10-30× higher sensitivity than detectors used in *Herschel*.[55] These revolutionary detectors and cold, low-emissivity optics are key innovations that together deliver the vast improvement in sensitivity to enable the PI science as well as a vibrant GO program with opportunities for new discovery across much of astrophysics.

4 Spacecraft

The PRIMA spacecraft will be provided by BAE Systems. It includes a bus, propulsion system, avionics, command and data handling and flight software (FSW), and telecommunications. It is the 12th build of the BAE Systems Large Configurable Platform (BCP) bus line. It features a large, body-fixed solar array doubling as a sun shade and providing thermal isolation. This yields efficient passive cooling on the cold side of the observatory, enabling cryogenic temperatures required for the payload. The high-heritage spacecraft subsystems provide generous margins to all PRIMA key performance parameters. With the thermally friendly Earth-Sun L2 halo orbit, the thermal requirements imposed by the payload can be met with a standard bus with few modifications. PRIMA treats the end-to-end thermal system as the heart of the architecture and one special provision is the use of low coefficient of thermal expansion structural bus elements. This minimizes thermal deformations under changes in sun angle and thereby enables stable pointing offsets between the ambient-temperature star trackers and the cold payload. PRIMA's total mass falls well below the 3375 kg launch vehicle capability given in the APEX Announcement of Opportunity. Major spacecraft subsystems are briefly described in the following six subsections.

4.1 Structures and Mechanisms

A hexagonal bus structure provides a direct load path from the conical launch vehicle adapter ring to the payload deck through six corner posts and directly to the payload bipod struts. The sun shade assembly interfaces with the hexagonal primary mirror structure to provide a load path to the launch vehicle adapter. The top deck of the spacecraft functions as the payload deck, minimizing thermal distortion between the star tracker assembly and the payload mounting interface. It connects to the structure via kinematic mounts, providing thermal isolation and structural compliance, with adequate stiffness to handle launch loads. PRIMA includes passive/damper-loaded hinges with release mechanisms for the two-panel sun-shade assembly, and a low-disturbance, two-axis high gain antenna gimbal that enables simultaneous science collection and two-way telecommunication.

4.2 Propulsion

PRIMA uses a monopropellant hydrazine blowdown system with a single AF-E-332 elastomeric reversible-diaphragm propellant tank aligned on the Z-axis to minimize center-of-gravity offsets in the lateral directions during the mission. Four 22-N thrusters located on the -Z face of the flight

system provide ΔV. Eight 1-N thrusters provide reaction control system functions with full redundancy, coupled about the Z-axis (boresight axis), and torque authority about the Y- and Z-axes. Thruster placement limits plume contamination of cold surfaces. The propulsion system is built directly on the bottom deck, facilitating parallel assembly and testing.

4.3 Avionics

The avionics architecture for PRIMA includes the command and data handling (C&DH; contributed by the Italian National Institute for Astrophysics, INAF), electrical power and distribution (EDPS), and attitude determination and control systems (ADCS). C&DH provides electrical interfaces, data processing, and data storage. These functions are performed by a block-redundant spacecraft control processor and an internally redundant command telemetry unit featuring a RAD510 single-board processor. Power is generated by the 14 m^2 sun shade-mounted solar array (2700 W at end of life, including 5-deg roll $+15$-deg pitch off-pointing) with GaAs cells with 32% efficiency. The EPDS is a direct energy transfer system with bus voltage regulated by the battery (26 to 34 V). Excess power remains on the array, with strings switched via the power control and distribution unit, and provides fault protection, including resettable overcurrent protection, bus voltage monitoring, and battery charge control. To minimize thermal distortion in the payload deck and <20% maximum battery depth of discharge during operations, most components are not power cycled.

The ADCS includes a scalable space inertial reference unit, coarse sun sensors, and reaction wheels. PRIMA's sub-arcsecond pointing stability and accuracy requirements are met with 150% and 39% margins, respectively. An onboard Kalman filter emphasizes gyro stability over short-time scales and long-term star tracker accuracy. Four optical heads observe distinct fields of view to produce small cross-boresight pointing offsets by averaging per star centroid biases. The star trackers are mounted directly to the thermally controlled payload deck to reduce offsets due to thermal distortion and star tracker mounting locations mitigate misalignment to the telescope's optical axis. Microvibrations from all spacecraft components are accounted for in the pointing error budget. Alignment calibration is performed for 45 min daily to maintain high-precision knowledge of the telescope-to-star tracker alignment using onboard processing. Reaction control system thrusters remove angular momentum created by solar pressure torque on a 3-day cadence. Sixteen coarse sun sensors provide redundant sun avoidance. Reaction wheels provide more than 3 days of momentum overhead while maintaining slew/settle capability of 180-deg about-sun reorientation in 12 min.

4.4 Command and Data Handling

The C&DH unit architecture is organized into three main blocks: (1) A power distribution block, with a separate board interfaced with the primary power lines from the spacecraft, including the power-conditioning components to provide both internal and external secondary power lines. (2) A data-handling block, based on the usage of a LEON GR740 quad-core processor, implementing all payload commanding and control functionalities. (3) A payload interface handling block, based on the usage of a radiation-tolerant, high-density field-programmable gate arrays (FPGA) implementing the control of the majority of the unit's external interfaces. The use of a complex SoC such as the GR740 and a high-density FPGA enables integrating all needed functionalities in a small volume and low mass.

4.5 Flight Software and Fault Management

PRIMA's spacecraft FSW retains a high reuse of code from years of BCP-based missions. There are two FSW images and one set of FSW tables stored in nonvolatile memory. The FSW interfaces with C&DH, ADCS, EPDS, and the payload hardware via the spacecraft control processor. Onboard fault management is implemented within FSW as a deterministic system consisting of configurable FSW and hardware responses to spacecraft anomalies. It provides automated detection and fault responses mapped to specific telemetry monitors in all major subsystems. All PRIMA-unique needs, including sun avoidance and thermal limits for any response, including safe mode, are met with the heritage system. All health and safety parameters are reconfigurable on orbit.

4.6 Telecommunications

The PRIMA telecommunications system is compatible with both the Near-Space Network (NSN) Lunar Exploration Ground Sites (LEGS) and Deep Space Network (DSN) for telecommand and telemetry support using X-band and science data downlink using Ka-band. This architecture includes a 140-W RF Ka-band traveling-wave tube amplifier, X/X/Ka-band integrated deep-space transponder that supports AES256 decryption for command uplink protection, a 0.7-m high-gain antenna (provided by INAF), 20-W RF X-band solid-state power amplifier, and 0.13-m medium gain antenna. The high-gain antenna is mounted on a two-axis gimbal to enable Ka-band downlink during observations. The medium-gain antenna is statically mounted to the bus for *X*-band command uplink and telemetry downlink. Earth-Sun L2 halo orbit design constraints determine the elevation and azimuth requirements for the gimbal (35-deg azimuth, 45-deg elevation). For launch, early operations, and safe mode, a set of patch low-gain antennas provides commanding and telemetry capability.

5 Payload

In this section, we describe each major system of PRIMA's payload, which resides entirely in a 4.5-K thermal zone. In Fig. 3, the light enters the telescope from the left and reflects off the 1.8-m primary to the secondary mirror, which has a focusing mechanism. The field is then split into two paths for FIRESS and PRIMAger. In each path a tertiary mirror collimates the light, then a beam-steering mirror (BSM) enables chopping and beam steering up to ± 17 arcmin on sky. The instruments are cooled to 1 K to minimize the thermal radiation background and the KIDs require 0.1 K temperature to operate. Cooling for both is provided by the CADR.

5.1 Optical Design

The PRIMA optical system includes a 1.8-m, 36× afocal telescope followed by the instruments (Fig. 4). The telescope is an obscured Korsch three-mirror anastigmat used off-axis in the field, such as the *JWST* and Roman Space Telescope designs. The Korsch three-mirror design combines immunity to low-order aberrations, a wide and flat field, and low obscuration. The three-mirror performance is required to meet wavefront error requirements over the full field subtended by both instruments, including the field accessed with their steering mirrors. The telescope collects light from across a 1.52 deg × 0.41 deg field of view and provides collimated beams to the

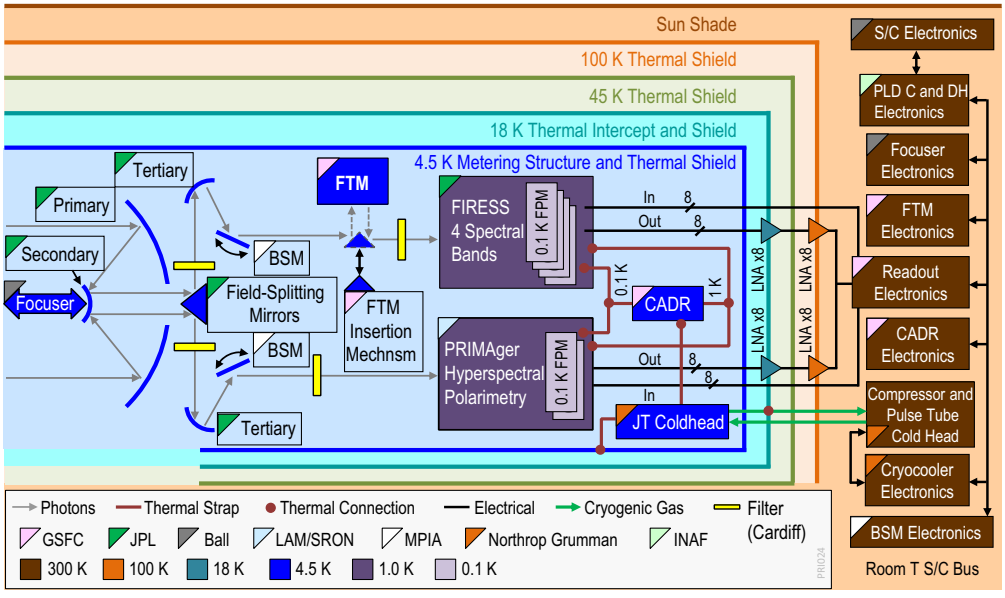

Fig. 3 Payload functional diagram with the main elements of the payload with arrows showing the light path in gray, colors illustrating the thermal structure, and brown boxes identifying the main electrical components. The triangular keys indicate which institution within the collaboration is responsible for each component.

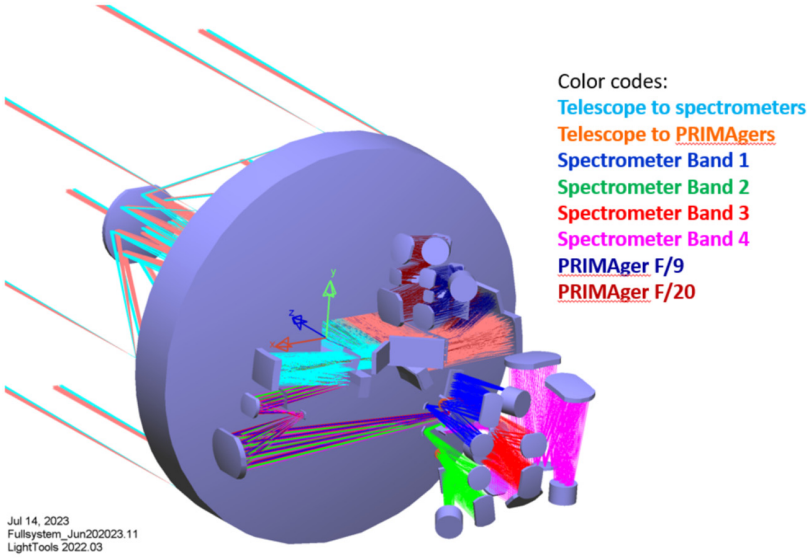

Fig. 4 PRIMA optics viewed from behind the primary mirror where the instruments reside. The ray colors indicate segments of the optical paths.

separate imager and spectrometer instruments. Before the internal telescope focus, separate flat fold mirrors for the spectrometer and imager divert the light to separate tertiary mirrors, which form collimated exit pupils for two scan mirrors.[56] The scan mirror sizes, tilt ranges, and bandwidths are in-family with those used in *Herschel*. Following each scan mirror is the minimum-complexity optical design for each instrument path. The telescope has a design wavefront error of less than 500 nm, including allocations for fabrication, alignment, cryo-deformation, and ground-support test equipment, bringing the total estimated as-built telescope wavefront error to 1.7 μm RMS at the worst field position. For details, see Ref. 57. Stray light is controlled with baffling internal to the payload and strict requirements on out-of-band filter transmission.

The spectrometer optical path consists of the FTM followed by four grating-based imaging spectrometers.[57] A pair of flat mirrors on a translation stage allow the FTM to be inserted or removed from the path depending on whether high- or low-resolution spectroscopy is needed. The imaging path consists of an f/9 and f/20 camera separated in the field. They are contributed by the Laboratoire d' Astrophysique de Marseille (LAM).

5.2 Beam Steering Mirrors

Two identical beam steering mirrors (Fig. 5) enable signal chopping and flexible mapping modes. These 57-mm aperture, two-axis mirrors build upon *Herschel* Photodetector Array Camera and

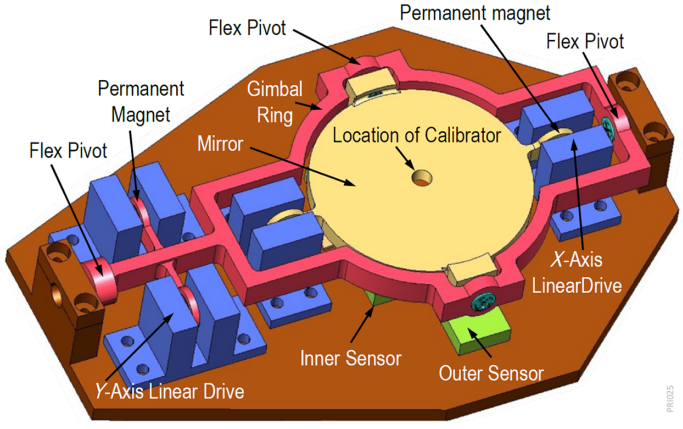

Fig. 5 Two-axis BSMs use *Herschel* PACS heritage and allow up to $\pm$17 arcmin steering on the sky, enabling PRIMA's scanning and chopping modes. Main components of the architecture are labeled.

Spectrometer (PACS) heritage.[58] Requirements and capabilities are two-axis motion covering up to ± 17 arcmin on the sky and a chopping angle up to 2.6 arcmin at 5 Hz with $\geq 85\%$ duty cycle. The mirror is located on a gimbal stage and suspended in both axes by two pairs of flex pivots. These monolithic pivots are fabricated with beryllium copper and provide enough lifetime for a large number of BSM motion cycles. The sensor system for closed-loop control consists of magneto-resistive field plates that are biased by permanent magnets located on the backside of the mirror. Each BSM is actuated by two pairs of DC motors based on the *Herschel* PACS chopper. They consist of stationary drive coils made of high-purity aluminum and NdFeB permanent magnets located on the mirror and gimbal assembly. The BSMs are provided by the Max Planck Institute for Astronomy (MPIA).

5.3 Thermomechanical Design and Cryogenics

To ensure that the photon background is dominated by the astrophysical—zodiacal and Galactic—sky emission across PRIMA's full bandpass, rather than from spacecraft self-emission, PRIMA's telescope and relay optics must be near 4.5 K. The instrument optics, particularly the far-IR spectrometers, must be kept at 1 K to prevent them from introducing thermal emission through the focal-plane filters. The baseline temperature requirement for the focal planes is 0.1 K to facilitate KID sensitivity. To meet these temperature control requirements, PRIMA uses a hybrid passive and active cryogenic thermal control system for efficient cooling. Two previous papers[59,60] provided detailed descriptions of the thermal system design and cryocooler risk reduction test. Here, we provide a summary of the design.

Taking advantage of the benign Sun-Earth Lagrange Point L2 thermal environment, PRIMA uses a multistage passive cooling system with thermal shields and radiators to reduce parasitic radiation loads on the cryogenic payload. The active cooling system uses a mechanical cryocooler to provide cooling at 18 K and 4.5 K and a CADR to provide cooling at 1.0 K and 0.1 K. The mechanical cooler has a strong heritage in the *JWST* MIRI cryocooler,[61] and the CADR has a heritage in *Hitomi*'s ADR system.[62] The PRIMA mechanical cooler is a pulse-tube/Joule-Thomson (PT/JT) hybrid cooler. The cryocooler uses flexure bearings and piston clearance seals, which have demonstrated service lifetimes of more than 20 years. The JT stage can provide remote distributed cooling for heat loads at 4.5 K spread across the instrument enclosure with nominal separation distances of 1 m. The JT stage also allows the PT precooler and the JT compressors to be remotely located inside the spacecraft bus to minimize the impact of its exported vibrations on instrument pointing accuracy. With this payload thermal architecture, the hybrid thermal control system can provide cooling power 2× the current best-estimated heat loads at temperatures below 18 K. As a class C mission, single-string control electronics are sufficient.

PRIMA uses a three-layer thermal shield subsystem to reduce the thermal radiation loads from the solar panel/sunshield and spacecraft bus on the cryogenic payload assembly. The outer (at $\sim$100 K) and middle (at $\sim$45 K) thermal shields are passively cooled while the inner shield at $\sim$18 K is actively cooled by the mechanical cryocooler. The geometry of the thermal shields is tailored to enable high-sensitivity science measurements and minimize parasitic loads into the payload during science operations. The cryogenic payload inside the actively cooled 18 K shield is supported by the spacecraft with bipods made of S-Glass composite in the 300 to 45 K region and T300 carbon fiber reinforced polymer in the 45 to 4.5 K. T-300 struts are also used to support 1.0 K instrument enclosures from the 4.5 K payload enclosure. A Kevlar suspension system is used to support each 0.1 K detector array from the 1.0 K enclosure.

We selected a hybrid cooler to achieve efficient cooling at 4.5 K using the existing MIRI TRL9 linear compressor and Stirling pulse tube cooler technologies.[60] PRIMA's hybrid cooler uses ^{3}He instead of ^{4}He as the working fluid for the JT stage. Using ^{3}He allows a JT restriction outlet pressure 2× greater than a JT stage using ^{4}He for 4.5 K cooling. The much higher compressor suction pressure not only increases the system mass flow rate but also the specific cooling capacity associated with the JT effect. The build of the PRIMA cooler will be accomplished by adding a parallel MIRI JT compressor into the existing spare flight MIRI JT stage. The three-stage pulse-tube precooler, the four JT recuperators, their interface with the pulse tube stage, the JT bypass valve, and potentially the JT restriction from the MIRI spare cooler will remain unchanged. Thus, the key subsystems and all key hardware components in the PRIMA cooler

are identical to those in the MIRI cooler, having the same high reliability and low exported vibration characteristics (although KIDs are not susceptible to microphonics like, e.g., high-impedance semiconductor bolometers).

To reduce the technical risk of the overall payload thermal system, we have measured compressor performance with ^{3}He under the PRIMA design condition using the MIRI development model compressor. Test results confirm (1) that the compressor can meet the PRIMA requirement for each compressor with a significant margin and (2) that the thermodynamic package used in the JT stage thermal analysis can reliably predict the JT stage cooling performance.

PRIMA uses a five-stage CADR that provides continuous cooling at 0.1 K and 1.0 K. Compared with a single-shot ADR, a CADR is lighter and smaller and has a much larger cooling capacity. The CADR has no mechanical moving parts and is designed for a minimum 10-year operating life. The PRIMA CADR is based on a four-stage CADR developed at GSFC and its control electronics are a copy of the cards used in *Hitomi* (technology readiness level 9) with two additional cold and warm ADR stage cards. A dedicated harness radiator is used to keep the warm end of the CADR high-temperature superconducting leads below 70 K, well below their critical temperature. The five-stage CADR is designed to provide cooling power of 9 μW at 100 mK and 700 μW at 1.0 K when the heat rejection at the 4.5 K interface is limited to 8 mW.

5.4 Instrumentation

5.4.1 *FIRESS*

The Far-Infrared Enhanced Survey Spectrometer (FIRESS) is a multimode spectrograph covering the 24 to 235 μm range. More details on the instrument design and performance can be found in Bradford et al. in this special issue. The FIRESS approach is driven by three basic principles that drive the design of both the low-resolution and high-resolution modes. First is sensitivity, which is critical for accomplishing the science in a timely manner, particularly the early universe extragalactic measurements. Ensuring zodiacal-light-limited performance places requirements on the detector performance, the efficiency of the optics, and the thermal design of the telescope and FIRESS itself. Second is wide-band coverage to enable measurement of the full suite of spectral features, and for sources at a range of redshifts, with as few separate observations as possible. This leads to the basic approach of four bands, each covering nearly an octave to span the full FIRESS range. Finally, some degree of spatial multiplexing, or mapping speed, is desired for ISM mapping and 3D line tomography; this drives the slit length and total array pixel format within the limitations of the available readout.

At the heart of FIRESS are four wideband grating modules spanning 24 to 43, 42 to 76, 74 to 134, and 130 to 235 μm (bands 1 to 4, respectively) with the full range covered instantaneously. Figure 6 shows the FIRESS slits as they map to the sky and the focal planes. Each band couples a slit on the sky through a first-order diffraction grating to a focal plane that has 24 spatial by 84 spectral KID pixels on a 900 μm pitch. The KIDs are arranged in two 12×84 pixel chips. The pixels are hexagonally packed so that every other spectral row is staggered by half a pixel to provide subpixel sampling by co-adding a source's spectrum as it is chopped or rastered into multiple spatial positions. The FIRESS grating modules provide resolving power $R = (\lambda/\delta\lambda)$ of $\sim$150; however, the pixel pitch is mapped to approximately $f\lambda$ (which varies across each band) so that the pixel size itself limits resolving power to as low as 85 to 95 at the short-wavelength end of each band.

In the current design, bands 1 and 2 are identical (except for the plate scale) with the design driven by band 2. This means that band 1 has larger spatial pixels than the beam size with spatial resolution traded in favor of mapping speed. Other than this unique aspect of band 1, the slit lengths and widths both scale with wavelength for bands 2, 3, and 4. Using dichroic beam splitters, the slits of the four bands are arranged so that bands 1 and 3 spatially overlap and bands 2 and 4 spatially overlap. This enables a continuous 24 to 235 μm FIRESS spectrum in two pointings of a point source.

For high-resolution spectroscopy, FIRESS uses the same four grating modules and their detector arrays but processes the light through the FTM as it travels from the telescope to the slits. This is implemented with a pair of mirrors on a sliding carriage that intercepts the beam and sends it into the FTM optics, then re-inserts the processed light into the beam directed toward the slits. This creates a post-dispersed Fourier Transform spectrometer (Fig. 7).

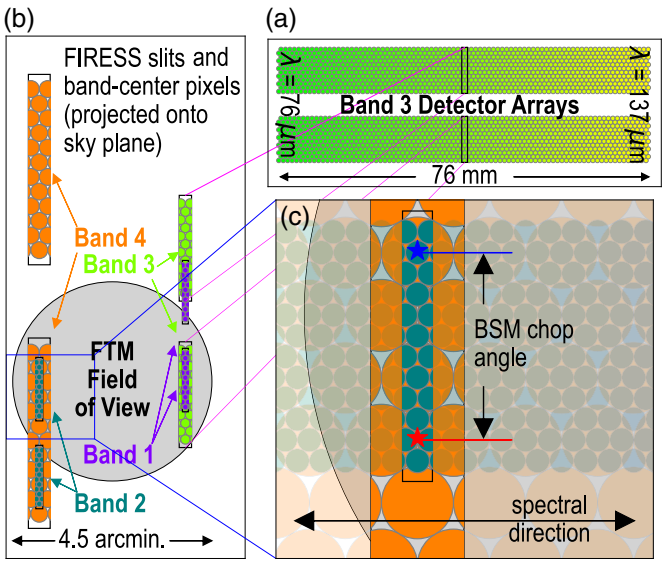

Fig. 6 FIRESS field of view and array format. Panel (a) shows one of the four idential detector arrays, each is 84 spectral (horizontal as shown) × 24 spatial (vertical as shown) = 1008 total pixels. Panel (b) shows the overlapping of bands 1 and 3 in one position, and bands 2 and 4 in the other position, so that an astrophysical source can be observed in all four bands with two observations. The field of view of the FTM is shown here as well; when engaged, it couples to a subset of all slits. Panel (c) shows the detail of the hexagonal pixel arrangement and the overlapping of bands 2 and 4. The red and blue stars denote example positions to which a source can be steered via chopping with the BSM.

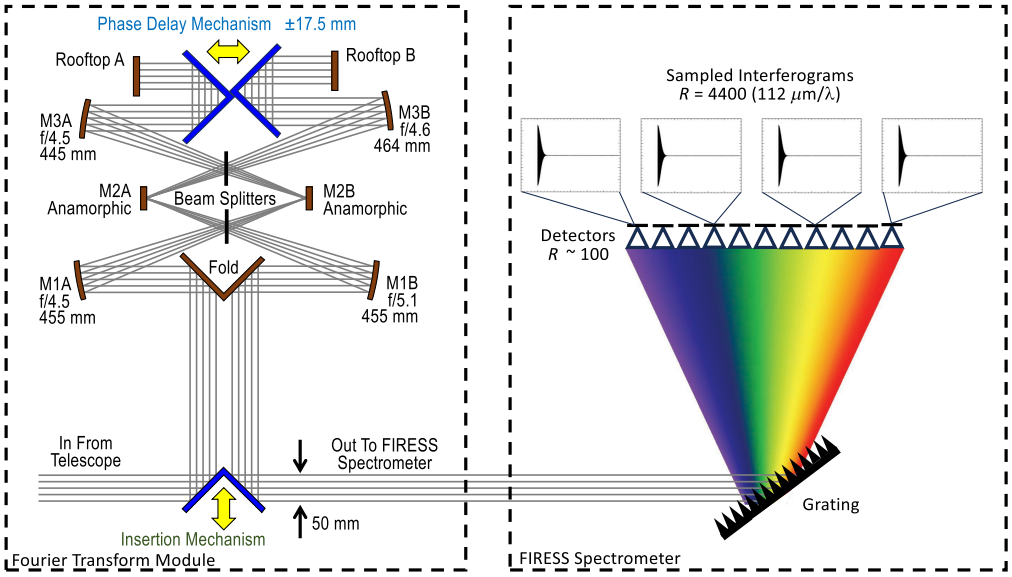

Fig. 7 FIRESS grating modules and Fourier Transform module create a post-dispersion Fourier Transform spectrometer to provide high spectral resolution with low optical loading. (*Left*) Schematic representation of the FTM beam path with the beam insertion mechanism at the bottom. (*Right*) Schematic representation of a single grating module, which can operate in low-resolution mode without the FTM or high-resolution mode with the FTM.

The FTM is a Martin-Puplett system in which a polarizing beam splitter consisting of 1 μm wide gold wires with 2 μm pitch micromachined on both sides of a 1-μm-thick polyimide film separates the incident beam into orthogonal polarizations. A second identical grid, clocked at 45 deg to the first, mixes the beams. The beam splitters will be produced by the Cardiff University Astronomy Instrumentation Group and have been successfully tested in a

post-dispersion FTS.[63,64] A double-flexure mechanism with 35-mm physical travel[65,66] and ×8 optical path length multiplier provides up to 240-mm optical phase delay with a 20-mm margin on either side. Flat rooftop mirrors route the phase-delayed beams back through the beam splitters to recombine before exiting to the FIRESS spectrometer, where the fringe pattern is sampled. Asymmetric arms place the exit pupil at its nominal position when the phase delay is mid-way through its stroke, reducing beam walk by a factor of two. As the phase delay mechanism moves from one end of its travel to the other, it produces a single-sided interferogram with frequency resolution $\Delta\nu = c/(2z_{\max})$, where $z_{\max}$ is the maximum optical phase delay. The PRIMA 240-mm optical phase delay produces channel width $\Delta\nu \sim 600$ MHz, corresponding to spectral resolution $R = 4400(112\ \mu\mathrm{m}/\lambda)$. Shorter throws can be used for lower-resolving power applications. With this design, the FTM interferes with one beam from the sky with a second beam from the detector. Because the focal planes are at 0.1 K, there is essentially no emission in the PRIMA bands, resulting in interferograms of only sky spectra.

Unlike a traditional Fourier Transform spectrometer, in which a single detector samples the interferogram over the full instrument passband, the FIRESS post-dispersed Fourier Transform spectrometer distributes the phase-delayed signal to multiple narrow-band detectors.[64] The Fourier Transform of the interferogram at each detector produces a high-resolution spectrum of the portion of the band that is covered by a single detector passband. The resulting set of spectra is then stitched together to produce a high-resolution spectrum covering the full instrumental passband.

The post-dispersed Fourier Transform spectrometer retains the high (tunable) spectral resolution of traditional broadband Fourier Transform spectroscopy but with advantages. The ∼1% fractional passband for each FIRESS detector limits the total power absorbed by each detector, producing an order-of-magnitude reduction in the photon noise from the astrophysical backgrounds. In addition, the reduced detector loading produces a corresponding reduction in the amplitude of the white-light null at zero path difference, relaxing requirements for dynamic range in the detector readout.

5.4.2 *PRIMAger*

PRIMAger is a mapping far-IR camera employing two focal planes of KIDs that observe simultaneously to cover the 24 to 261 μm range. See Ciesla et al. (this volume) for a full description of the instrument. The key features of this instrument are (1) mapping speed, angular resolution, and spectral sampling sufficient to generate large far-IR-selected samples of galaxies at cosmic noon; (2) spectrophotometric wavelength coverage and resolution sufficient to detect PAH emission bands at cosmic noon; and (3) sensitivity to the fractional linear polarization of dust emission in multiple far-IR bands that probe the nature of dust grains. Although not part of the PI science program, the mapping of the magnetic field structure of nearby galaxies will be enabled by polarimetry.

The hyperspectral focal plane (PRIMAger Hyperspectral Imager; PHI), composed of two arrays of lens-absorber-coupled hybrid KIDs, covers the 24 to 84 μm range with a spectral resolution of $R \sim 8$. Linearly variable filters (LVFs) placed above the KID arrays provide $R \sim 8$ as a gradient of bandpass centroid wavelength along one axis of the detector array. The polarimetric focal plane (PRIMAger Polarimetric Imager; PPI), covering the 80 to 261 μm range with four filters ($R = 4$), has lens-antenna-coupled hybrid KIDs. Each pixel is sensitive to one out of three angles of linear polarization, and together, they measure the I, Q, and U Stokes parameters.

The hyperspectral and polarimetric focal planes share the PRIMAger field-of-view and are separated by 16 arcmin projected onto the sky (Fig. 8). The BSM enables rapid, two-dimensional scanning of the instrument field-of-view within the 42 arcmin × 24 arcmin telescope field of view. Larger areas are mapped by combining this motion with observatory slewing. Although each detector images a different part of the PRIMAger field of view, the scanning strategy ensures that a common sky area can be mapped by all detectors.

The opto-mechanical design of the PRIMAger instrument consists of primary Aluminum 6061 T6 boxes operating at 1 K. The two focal planes, including the detector systems operating at 0.1 K, are linked to the main boxes via nonconductive hexapods ensuring the required thermal decoupling between 1 K and 0.1 K stages. The light of the PHI and PPI imagers follow different paths with similar optical architectures composed of four aluminum mirrors. The PHI imager is

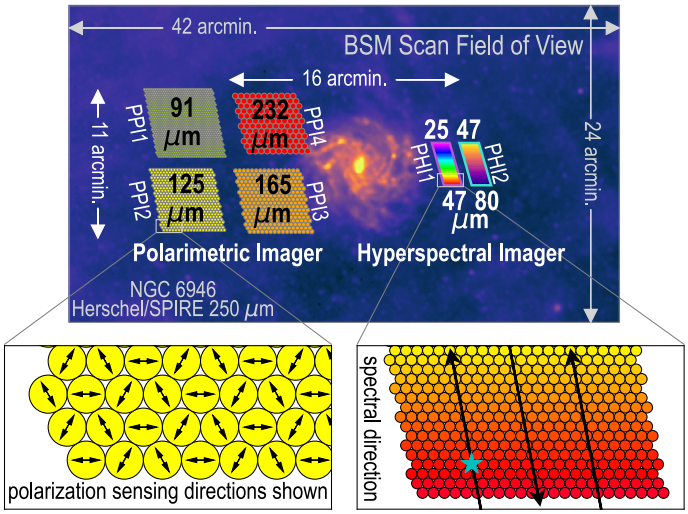

Fig. 8 (*Top*) Field of view covered by PRIMAger. The imprint of the PHI (PHI1 and PHI2) and PPI (PP1, PP2, PP3, and PPI4) focal planes on the sky are shown. From center to center, they are separated by 16 arcmin. The beam steering mirror enables coverage of a larger area, corresponding to the entire rectangle shown on the *Herschel*/SPIRE image of NGC 6946. (*Lower left*) Schemating showing how each pixel of the PPI detectors is sensitive to one linear polarization angle. (*Lower right*) Along a horizontal row, each detector of the PHI is sensitive to a waveband determined by the linearly variable filter. The black arrows show the directions of scan and the blue star represents an astronomical source whose spectral energy distribution is measured when it is scanned over the detector array along the arrow.

f/20 and the PPI imager is f/9. The PHI image quality is quasi diffraction-limited, whereas the PPI image quality is diffraction-limited.

The quasi-optical radiation filters in PRIMAger have low-pass filters deployed at 4.5 K, 1 K, and 0.1 K, successively blocking IR and far-IR out-of-band radiation and limiting the power reaching the detectors. This filtering uses the long-standing metal-mesh technology of Cardiff University,[67] previously deployed on both *Herschel* PACS and SPIRE instruments.[68] A combination of high-pass and low-pass filters block out-of-band radiation and bandpass filters define the bands at the focal planes. The combined throughput from the filter chain aims to meet a requirement of no worse than 55% while also reducing out-of-band (IR) radiation to 1 part in 10^{-10}. The two focal planes are magnetically shielded and thermal shielding isolates the focal planes from thermal radiation inside the 4.5 K radiative environment.

The Linear Variable Filters (LVFs) planned for PRIMAger build upon the established technology of resonant metal-mesh structures,[67] similar to other filter technologies utilized in PRIMA. The spectral response of each LVF varies linearly along one axis of the array. Dual-layer scale models at 200 and 375 μm have demonstrated the targeted bandpass characteristics, resolving power, and in-band transmission. Spectral measurements of single-layer prototypes for the shortwave PRIMAger band (PHI1) show excellent agreement with simulation results. SRON has developed prototypes demonstrating graded spectral resolution of $\sim R \sim 8$ for representatively sized filters covering the 25 to 45 μm band. Optimized designs achieving $R \sim 10$ at the short-wavelength limit, while satisfying bandwidth and transmission requirements, have been finalized and are currently being implemented. The robustness of this technology has been confirmed through successful vibration, shock, and thermal-cycle testing. The remaining advanced engineering tasks include integrating the filters with MKID detector arrays, implementing improved substrate materials, experimentally validating the final design, and further optimizing out-of-band performance.

5.4.3 *KIDs: the innovation enabling scientific breakthrough*

KIDs are a relatively new type of detector; therefore, we summarize their operational principles prior to describing PRIMA's KIDs. In a superconducting material, two types of charge carriers are present. One type is Cooper pairs: paired electrons in a single quantum state at the Fermi

energy that transport charge without any resistance but with a finite inductive response caused by the finite mass of the electrons. The second is quasiparticles: at finite temperatures thermal excitations exist, called quasiparticles, whose charge transport is resistive. As a consequence, the electrodynamic response of a superconductor is described by a complex surface impedance $\sigma = \sigma_1 - i\sigma_2$, where σ_1 represents the resistive response from quasiparticles and σ_2 represents the inductive response from the Cooper pairs.

In 2002, both Sergeev et al.[69] and Day et al.[16] realized that it is possible to create a very sensitive radiation detector when operating a superconductor at $T \ll T_c$: Radiation impinging on a superconducting material can be absorbed when the radiation frequency $f \geq 2\Delta/h \simeq 90$ GHz for aluminum. Here, $\Delta = 1.76 k_B T c$ is the superconducting energy gap, h is Planck's constant, and k_B is Boltzmann's constant. Radiation absorption results in breaking Cooper pairs into quasiparticles, causing a small change in σ that is proportional to the quasiparticle density $n_{\rm qp}$ in the superconductor. Day et al.[16] proposed to sense these small changes in $\sigma(n_{\rm qp})$ using a planar resonator, with a typical resonant frequency $f_{\rm Res}$ of 0.2–8 GHz. Importantly, the resonator frequency responsivity, $df_{\rm Res}/dn_{\rm qp}$, is dependent only on the resonator design and materials. The strength of this approach is that the minimum possible resonator bandwidth is ${\rm BW} = Q_i/f_{\rm Res}$, with $Q_i = \tan(\delta^{-1})$, where $\tan(\delta^{-1})$ is loss tangent, which is inversely proportional to the quasiparticle density and exceeds 10^6 at $T \ll T_c$. So, at $T \ll T_c$, the resonator frequency response can be a measurable fraction of the resonator bandwidth even if the change in $n_{\rm qp}$ is very small. Another practical advantage is that many resonators can be designed sensitive to the same radiation, but each with a different value of $f_{\rm Res}$ and all connected to the same readout line. Chips with hundreds or thousands of resonators can therefore be read out using a single coaxial cable pair and room temperature back-end.

In many cases, modern KIDs use a combination of two materials, one with a high T_c to create the resonator geometry and one with a low T_c material at the inductive end of the resonator where radiation absorption takes place. Quasiparticles created there are confined by the higher energy gap of the surrounding high T_c material,[70] thereby maximizing response. The capacitive portion of the resonator is designed to minimize excess noise originating from dielectric disorder, as first described by Gao et al.[71] For PRIMA, aluminum is used as the photo-sensitive material because this material has proven to yield by far the best sensitivity.[18,72]

5.4.4 *PRIMA KIDs in context*

Sensitive far-IR detectors have been developed by the astrophysics community. Multiple approaches have been pursued over the past decades, and our team members have been involved in several of these efforts. PRIMA has baselined KIDs, but another leading approach has been transition-edge-sensor (TES) bolometers with SQUID-multiplexed readouts[73]; TESs are promising given their success with relatively large arrays in microwave-background experiments[74–76] and far-IR imaging instruments.[77,78] TES bolometers were pushed toward the 10^{-19} W Hz$^{-1/2}$ noise-equivalent-power (NEP) requirement for spectroscopy on a cryogenic space mission such as PRIMA[79–85] and would be a credible approach for PRIMA. However, in the last 3 to 5 years, KIDs have emerged as a preferred approach for a few reasons. First, KIDs have demonstrated better sensitivities, with measured NEP now well below 10^{-19} WHz$^{-1/2}$.[18,72] Crucially, this sensitivity comes with ample speed (response times on order 1 ms), as opposed to ultra-sensitive TES bolometers, which are typically much slower. Second, KIDs are easier to implement into large arrays because there are no active components in the cold readout, unlike TESs that have active SQUIDs in all multiplexing schemes. Finally, KIDs are more benign in their requirements levied on the system: operating temperatures can be 100 mK instead of 50 mK, and KIDs are not susceptible to radiation below the pair-breaking energy (90 GHz for aluminum), substantially simplifying the RF rejection requirements.

Relative to the KIDs used in ground-based and balloon-borne experiments,[86–88] the PRIMA KIDs must be more sensitive: factors of 10 to 100 in per-pixel NEP. However, this basic pixel sensitivity has already been demonstrated[18,72] and array formats and the readout frequency ranges are similar to those already demonstrated. PRIMA's KID technology development plan is designed to ensure that KIDs reach technology readiness level 6, including sensitivities, yield, cosmic ray mitigation, aging, and environmental factors, such as robustness against launch vibrations, prior to the preliminary design review.

5.4.5 *Dual-polarization absorber-coupled KIDs*

PRIMA will use two basic KID architectures. For the FIRESS arrays being developed at JPL, and the PRIMAger hyperspectral focal plane chips under development at SRON, we use absorber-coupled lumped-element KIDs. The term lumped-element refers to the separation of the inductor, which is the optically active element and must absorb the radiation, and the capacitor, which sets the readout frequency for each pixel. In these lumped-element KID arrays, all pixels have the same inductor/absorber and the capacitors are varied to create the range of readout frequencies. The inductor/absorber is a meandered aluminum trace patterned in thin (30 to 40 nm) aluminum film; its shape is carefully designed to meet two competing requirements: high absorption efficiency to the incident radiation and small total aluminum volume to maximize the response to absorbed power. As an example, some of the FIRESS prototype KIDs have inductors with a volume of 11 μm^3 and achieve NEP below 10^{-19} $WHz^{-1/2}$. The absorber shape is designed in conjunction with the lens profile to couple well to a given system f/# from the instrument optics, though this optimization is more forgiving than for antenna-coupled KIDs because the absorber-coupled pixels can be sensitive to many photon modes, similar to a traditional optical-wavelength detector pixel. In general, the highest efficiencies are obtained with slightly resonant designs, which have some wavelength dependence, so the pixel designs are wavelength-specific. A further description and pictures of some of our absorber-coupled KID devices can be found in our recent publications on PRIMA prototypes.[18,89–91] We further highlight an additional critical element for PRIMA's high-performance KID system: the microlens arrays which are hybridized with the KID arrays. In the case of FIRESS, a grayscale etching process for lens production, and a hybridization technique has been successfully developed at GSFC in parallel with the development of the JPL detector arrays. Further details can be found in Ref. 92.

5.4.6 *Linearly polarized antenna-coupled KIDs*

The PRIMAger Polarimeter Instrument (PPI) uses a focal plane array with polarization-sensitive KIDs. The polarization angle is rotated by 120 deg between pixels, enabling measurement of Stokes I, Q, and U in single scans of the telescope or BSM.[93] Figure 9(a) is a micrograph of a small-scale prototype device, photographed from the chip backside so that only the antenna structures (which are fabricated on 100-nm SiN membranes) are visible. The KIDs themselves are similar to those described in Ref. 72. The inset of Fig. 9(c) is a photograph of a single detector from the same device as shown in Fig. 9(a) but photographed from the front side. The light area

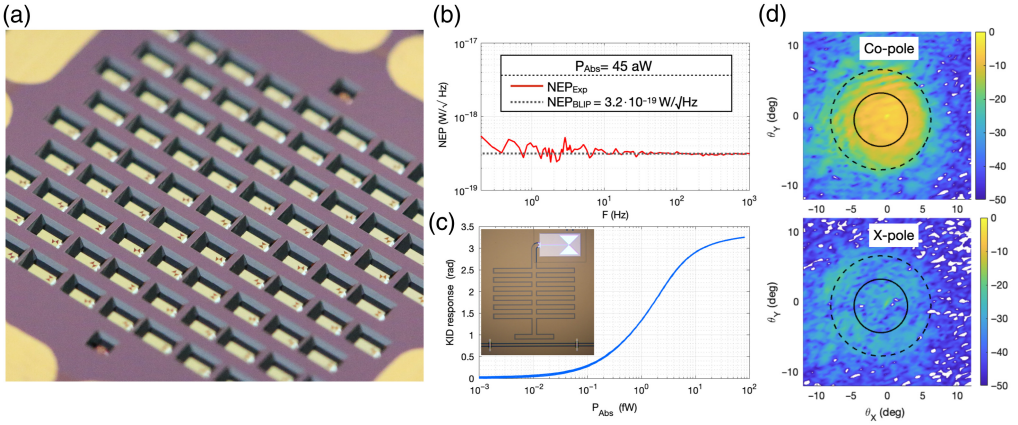

Fig. 9 (a) Optical micrograph of a PRIMAger polarimeter prototype KID array with the clocking of the antennas in 120-deg steps between pixels to enable polarimetry. This image is taken from the chip backside, showing only the radiation-sensitive part of the detectors. Microlenses will be bonded to the front of the array and illuminate the KIDs through the substrate. (b) Measured NEP at a PRIMA-relevant loading power of 45 aW (NEP_{Exp}, red line) and the calculated photon noise-limited NEP (NEP_{BLIP}, dotted gray line). (c) Response of a KID for increasing power incident on the detector. The inset shows a KID with the bowtie antenna and capacitive coupling to the readout line. (d) Pupil plane co- and cross-polarization beam patterns of a single pixel as shown in the inset of panel (c). The color bar scale is dB. The solid circles indicate the PRIMAger pupil size and the dashed lines indicate the experimental measurement setup pupil.

with the bowtie-shaped antenna couples to radiation. Under operation, a lens array is mounted on the chip metallization side with a vacuum gap of 4 μm created using Perminex pillars. For more details see Ref. 72.

When observing dark sky, the power received by the detectors in the PPI ranges from 35 to 90 attowatts (aW $= 10^{-18}$ W), increasing with decreasing frequency. However, when scanning relevant astronomical fields, the power incident on the detectors can be up to tens or even hundreds of femtowatts (fW $= 10^{-15}$ W). Therefore, the primary requirements for these detectors are (1) the KIDs exhibit photon noise-limited performance (BLIP), where the NEP is dominated by the noise equivalent power from photon arrival-rate fluctuations at the absorbed power P_{abs} relevant for the astrophysical observations. This photon noise-limited NEP is given by $\mathrm{NEP}_{\mathrm{ph}}^2 \simeq 2P_{\mathrm{abs}}hf$. Here, f is the band center frequency.[72] (2) The KIDs must remain operational at loading powers in the high fW range. (3) The KIDs have a low cross-polarization level—below −20 dB.

We fabricated and tested a set of KID arrays using the same fabrication recipe, array design, and integration with a small lens array of identical design as described in Ref. 72. The only exception is that we use an aluminum layer 40-nm thick instead of 16 nm to increase the dynamic range of the device. In the first experiment with the same setup as in Ref. 72, we measured the detector NEP at an absorbed power of 45 aW at 1.5 THz using a bandpass-filtered thermal load. This is done by first measuring the noise at a stable radiator temperature and subsequently by measuring the response due to a small temperature variation of the radiator.[72] In Fig. 9(b), the resulting NEP at an absorbed power of $P_{\mathrm{Abs}} = 45$ aW is shown together with the calculated $\mathrm{NEP}_{\mathrm{ph}}$. We observe that the KIDs are indeed background-limited, with only a slight $1/f$ contribution well below 1 Hz.

KIDs are inherently robust to dynamic range concerns in that their sensitivity degrades slowly as they begin to "saturate" and reduced sensitivity is usually required for bright sources. The challenge is that the resonances will move away from the readout probe tones (reducing sensitivity). PRIMA's KIDs will be in this regime for the brightest Galactic sources. PRIMA will have calibrators for both FIRESS and PRIMAger to calibrate the detector nonlinearities so that bright sources can be observed. To evaluate the dynamic range, the same experiment as above was repeated but with increased radiator temperature to tens of K to yield an absorbed power close to 100 fW [Fig. 9(c)]. The device response diminishes but does not completely vanish, at powers up to 100 fW, representing a dynamic range of more than a factor 1000. Further improvements are possible: (1) by replacing the interdigitated capacitor structure as shown in the inset of Fig. 9(c) with a meandering coplanar waveguide line, which will increase the dynamic range by a factor of 3 due to a reduction of the kinetic inductance fraction, and (2) by adding an additional readout tone placed at a frequency about one bandwidth below the $P_{\mathrm{Abs}} =$ 45 aW resonant frequency. This approach would also work for the absorber-coupled KIDs and a feasibility trade study is being conducted.

Finally, the co- and cross-polarization beam pattern was measured, as described in Ref. 94. The detector chip was mounted in a cryostat equipped with cold radiation attenuators that enable a beam-pattern measurement using scanned coherent sources at room temperature.[95] In Fig. 9(d), the co- and cross-polarization beam patterns propagate to the system pupil plane; the dashed circle shows the system pupil area, and the solid circles show the PRIMA pupil plane assuming a sampling of $1f\lambda$ and a focal ratio $f/\# = 7.5$. The cross-polarization level integrated over the PRIMAger pupil (solid circles) is −22 dB.

5.4.7 *KID readout electronics*

KID arrays are read out with a comb of probe tone frequencies, each one corresponding to one of the unique microresonators, with many tones per in/out coaxial cable pair and amplifier. PRIMA's readout electronics, developed by NASA/GSFC, are shared by FIRESS and PRIMAger via radio-frequency (RF) switching with one instrument operating at a time. In each of the eight signal chains, the comb of tones is synthesized via a weighted overlap-and-add (WOLA) linear time-varying polyphase filterbank (PFB) inverse fast Fourier transform (IFFT) on a Xilinx Kintex KU060 Ultrascale FPGA. The comb is converted to analog and sent through coaxial cables to the KID arrays. After interacting with the KID array, the modified comb returns through coaxial cables with amplification by low-noise amplifiers (LNAs) at 18 K and 100 K. Figure 10 shows the

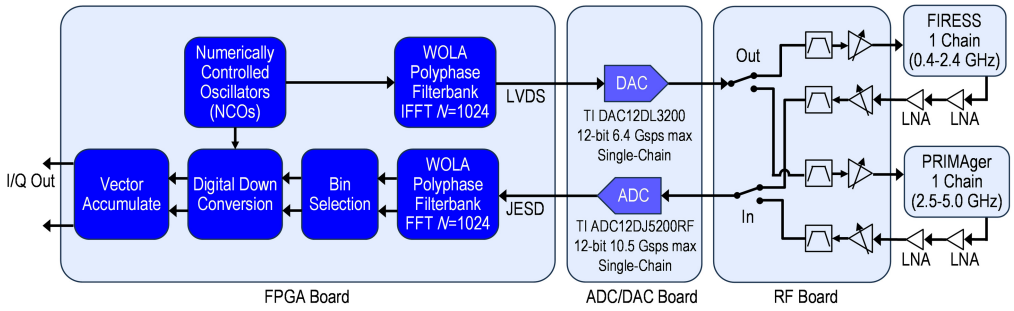

Fig. 10 Block diagram of a single PRIMA KID readout chain. The full complement of eight chains are switched between FIRESS and PRIMAger with filtering to enable readout of FIRESS in the first Nyquist zone and PRIMAger in the second Nyquist zone of the ADC and DAC when sampling at 5 Gsps. A high-heritage SpaceCube Mini v3.0 board (labeled "FPGA Board") houses a Xilinx Kintex Ultrascale KU060 FPGA and has high-speed interfaces with the ADC/DAC digitizer board. The RF electronics provide switching between the two instruments, filtering, and adjustment of overall gain for system noise optimization.

signal flow in a single readout chain. The algorithms have been used for over a decade, including in ground-based and balloon-borne instruments.[96,97]

The current plan is for ADC and DAC rates of 5 giga-samples per second (Gsps) to place the FIRESS readout band of 0.4 to 2.4 GHz in the first Nyquist zone and the PRIMAger 2.5 to 5.0 GHz readout band in the second Nyquist zone. An RF board provides switching between FIRESS and PRIMAger, with filtering for band selection and variable gain to set outgoing tone powers. Modular digital readout electronics use high-heritage SpaceCube boards.[98–103] The SpaceCube Mini v3.0 FPGA board and associated power supply cards are build-to-print and currently flying on the STP-H9-SCENIC mission on the ISS.[104] PRIMA requires a custom ADC/DAC board, backplane, and enclosure, which are adaptations of existing designs.[105,106]

6 Operations and Observing Modes

6.1 Operations

The PRIMA operational mission is at least 5 years in orbit at Sun-Earth L2. This orbit provides the spacecraft with a thermally stable platform for the cryogenic payload to operate continuously without the complications of eclipses that would be present in Earth's orbit. PRIMA can observe in any part of the sky at least once every six months.

PRIMA makes observations during a large percentage of each day with minimal time to slew between targets, including during the daily contacts with the ground. The spacecraft maps areas of sky or holds a steady attitude while staring at targets for significant periods of time. The observatory maintains strict sun-avoidance requirements to allow for continuous observations without stressing the cryogenic system. Daily stability calibrations provide accurate and precise knowledge of the pointing. Observation requests are uplinked up to a few times per week and processed from both principal investigator and general observer science programs for optimal observing efficiency.

6.2 Onboard Data Handling and Telemetry

Onboard data handling is provided by the C&DH computer, which interfaces between the scientific payload and the spacecraft and provides onboard memory. The most demanding functionality of the unit is the handling of the science data. With 10 kHz raw data acquisition rates for FIRESS and PRIMAger (in both in-phase and quadrature signal components) from up to 8000 KIDs (as during FIRESS observations), onboard preprocessing has to be implemented to keep the output data rate within the available budget fixed at 2.4 Tb/day. Cosmic ray events are removed and logarithmic regridding and data decimation algorithms are applied to obtain the final electrical time stream (df/f) for all KIDs. Thus, the aim of the onboard preprocessing is to obtain an average sample rate of 200 Hz for 8000 KIDs. These maximum rates lead to an expected data production of 28 Mbps, corresponding to ~1.8 T bits/day, assuming 18 h of

observation per day. This provides >30% margin on the maximum allowed data volume. The downlink to the ground assumes a rate of 140 Mbps over a total average of 5 h/day. Early in the mission and as necessary throughout, it will be possible to record and downlink short segments (several seconds) of full-rate data from the KID arrays for diagnostic purposes. This will allow verification of the cosmic ray removal and downsampling algorithms, as well as the detailed characteristics of the electronic noise; we expect it will be needed only rarely once commissioning is complete.

To support the assumed rate, a two-data-path telecommunication system is designed, including an *X*-band path for receiving commands and transmitting engineering data, and a Ka-band path for science data. An integrated deep-space transponder supports both channels with a high-gain antenna used for high data-rate communications. This design is inherited by a similar approach adopted for the VERITAS mission. It enables simultaneous dual-band capability with X-uplink/X-downlink and Ka-uplink/Ka-downlink.

6.3 Observing Modes

PRIMA's observing modes incorporate astrophysical signal modulation because (1) the KIDs are differential detectors and (2) place the signal band at frequencies above the detector $1/f$ noise.[107] PRIMAger has one observing mode: scan mapping with the size of the map being the defining parameter. Scan mapping modulates the input signal with observatory motion and/or with the BSM in a raster or Lissajous pattern. PRIMAger has two parallel fields, hyperspectral and polarimetric broad bands, that are mapped in unison. To get full spectral coverage for a PRIMAger observation, the mapped area must be larger than the separation of the two parallel fields.

FIRESS has three observing modes: low-resolution spectroscopy, low-resolution spectral scan mapping, and high-resolution spectroscopy. Low-resolution spectroscopy of point sources is chopped along the slit using the BSM for signal modulation. To obtain full spectral coverage, the point source is measured twice: one in each set of confocal bands (bands 1 and 3 and bands 2 and 4). For the low-resolution mapping mode, signal modulation is accomplished with a combination of observatory motion and/or BSM movements in a raster or Lissajous pattern. Full-spectral coverage is accomplished for sufficiently large maps that cover the two sets of confocal slits. High-resolution spectroscopy is for point sources with the FTM scanning phase modulator providing the signal modulation. For full-spectral coverage, two observations are required, one in each confocal set of bands.

6.4 Observation Planning and Scheduling

The PRIMA Science Center, operated by IPAC, develops the PRIMA planning and scheduling system leveraging heritage from *Spitzer* and *Herschel* (e.g., SPOT, HSpot). This system is used by scientists to plan PRIMA observations by inputing basic target properties (e.g., target ID, coordinates, and brightness) selecting the instrument, observing modes, and basic observing parameters (e.g., on-target and background exposure times, map dimensions, and dithering strategies) and placing observing constraints (e.g., grouping or sequencing of specific observations to provide accurate background subtraction or avoid saturation) where necessary. The inputs are used by the planning software to determine all possible observing windows for the target based on the PRIMA orbit and orientation constraints, to estimate on-target science and total ("wall clock") times, including instrument and observatory overheads, and to estimate downlink data volumes. Outputs include all observational parameters and command sequences needed to construct a unique observing sequence suitable for long-term planning and short-term scheduling of the observation. They can also be used to create a visualization of the PRIMA observation on the sky.

6.5 Science Data Processing

Processing of level 1 (de-trended raw data with common modes removed), level 2 (spectrophotometrically calibrated timestreams), and level 3 (basic calibrated data [BCDs] including maps, cubes, and stitched spectra) is done by IPAC for all FIRESS and PRIMAger science data. All L1-L3 data products are delivered to the PRIMA data archive constructed and hosted by IRSA. PRIMA data in the IRSA archive will be co-located with a large number of NASA mission datasets (e.g., survey and pointed datasets from *IRAS*, *Spitzer*, 2MASS, *WISE*, *Euclid*, *SOFIA*,

and *Planck*) and take full advantage of a suite of powerful data visualization and analysis tools. Calibration reference files (e.g., dispersion solutions, flat fields, distortion corrections, darks, relative and absolute photometric calibration, and point spread functions), which are used by the science pipeline in the calibration of the level 3 science data, are produced in a parallel, asynchronous calibration pipeline. The calibration pipeline shares many of the initial processing steps of the science pipeline, because astrophysical sources are primarily used for calibration in orbit, but additionally produces reference files needed by the science pipeline as inputs.

Level 4 data science data products (extracted spectra and catalogs, spectral feature fluxes, derived astrophysical quantities, etc.) necessary to meet the principal investigator science objectives are produced by the PRIMA science team and similarly delivered to IRSA. The PRIMA science team delivers algorithms and software to IPAC for incorporation into the PRIMA automated science data and calibration pipelines, as well as an initial set of calibration reference files for the science data pipeline based on ground test data.

FIRESS low-resolution and PRIMAger data share many components of the science data pipeline through the creation of maps and spectral data cubes (level 3). The FIRESS high-resolution science data pipeline contains additional steps, such as interferogram inversion and grating channel stitching, to produce the level 3 data products.

7 Conclusion

PRIMA is designed to meet the ambitious science goals of a far-IR Probe as outlined in Astro2020. It does this by taking advantage of recent KID technology maturation coupled with a 4.5 K telescope to minimize photon noise (from the telescope and optics). PRIMA's KIDs already meet its NEP requirements and flight-size prototype arrays are in production and testing. Cooling is provided by a cryocooler with JWST heritage and a CADR for 0.1 K focal plane arrays. The optics feed instruments that provide: (1) imaging with spectral energy distribution data cubes and polarimetry and (2) dispersive spectroscopy for low-resolution, with a Fourier Transform module mode for high-resolution spectroscopy. The spacecraft uses the high-heritage BAE Systems Large Configurable Platform. Each of these subsystems were briefly described with citations given for topical papers in this special journal section with in-depth descriptions. PRIMA's implementation schedule culminates in a 2031 launch to an Earth–Sun L2 halo orbit and commencement of science observations. Twenty-five percent of observing time will be devoted to principal investigator science and 75% will be for NASA-supported guest-observer science.

Disclosures

The authors declare that there are no financial interests, commercial affiliations, or other potential conflicts of interest that could have influenced the objectivity of this research or the writing of this paper.

Code and Data Availability

Data used in this generation of this paper and not cited in references in the paper include detailed PRIMA engineering design data that are PRIMA and JPL proprietary and thus not available.

Acknowledgments

The authors wish to thank numerous colleagues for useful discussions leading to the development of the PRIMA concept. Those whose discussions have been particularly helpful but who do not appear on the author lists of PRIMA papers in this JATIS special issue include Jeff Booth, Lawrence Hahn, Keith Jahoda, Charles Lawrence, Dave Richardson, and Joe Sauvageau. We apologize for any omissions. The authors gratefully acknowledge support NASA SAT (Grant No. 80NSSC19K0489) for the KIDs and microlens arrays. This research was carried out in part at the Jet Propulsion Laboratory, California Institute of Technology, under a contract with the National Aeronautics and Space Administration (Grant No. 80NM0018D0004).

References

1. National Academies of Sciences, Engineering, and Medicine, *Pathways to Discovery in Astronomy and Astrophysics for the 2020s*, The National Academies Press, Washington, DC (2021).
2. B. P. Crill et al., "SPHEREx: NASA's near-infrared spectrophotometric all-sky survey," *Proc. SPIE* **11443**, 114430I (2020).
3. J. P. Gardner et al., "The James Webb Space Telescope Mission," *Publ. Astron. Soc. Pac.* **135**, 068001 (2023).
4. L. Feinberg et al., "The Habitable Worlds Observatory engineering view: status, plans, and opportunities," *Proc. SPIE* **13092**, 130921N (2024).
5. G. Neugebauer et al., "The Infrared Astronomical Satellite (IRAS) mission," *Astrophys. J.* **278**, L1–L6 (1984).
6. M. F. Kessler et al., "The Infrared Space Observatory (ISO) mission," *Astron. Astrophys.* **315**(2), L27–L31 (1996).
7. M. W. Werner et al., "The Spitzer space telescope mission," *Astrophys. J. Suppl. Ser.* **154**, 1–9 (2004).
8. H. Murakami et al., "The Infrared Astronomical Mission AKARI," *Publ. Astron. Soc. Jpn.* **59**, S369–S376 (2007).
9. G. L. Pilbratt et al., "Herschel Space Observatory. An ESA facility for far-infrared and submillimetre astronomy," *Astron. Astrophys.* **518**, L1 (2010).
10. R. D. Gehrz et al., "Status of the stratospheric observatory for infrared astronomy (SOFIA)," *Adv. Space Res.* **48**, 1004–1016 (2011).
11. P. R. Roelfsema et al., "SPICA-A large cryogenic infrared space telescope: unveiling the obscured universe," *Publ. Astron. Soc. Aust.* **35**, e030 (2018).
12. J. Glenn et al., "Galaxy evolution probe," *J. Astron. Telesc. Instrum. Syst.* **7**, 034004 (2021).
13. M. Meixner et al., "Origins space telescope science drivers to design traceability," *J. Astron. Telesc. Instrum. Syst.* **7**, 011012 (2021).
14. D. Leisawitz et al., "Origins space telescope: baseline mission concept," *J. Astron. Telesc. Instrum. Syst.* **7**(1), 011002 (2021).
15. P. K. Day et al., "A broadband superconducting detector suitable for use in large arrays," *Nature* **425**, 817–821 (2003).
16. P. K. Day et al., "Antenna-coupled microwave kinetic inductance detectors," *Nucl. Instrum. Methods Phys. Res. A* **559**, 561–563 (2006).
17. P. K. Day et al., "A 25-micrometer single-photon-sensitive kinetic inductance detector," *Phys. Rev. X* **14**, 041005 (2024).
18. M. Griffin et al., "SPACEKIDS: kinetic inductance detectors for space applications," *Proc. SPIE* **9914**, 991407 (2016).
19. J. Sayers et al., "Peculiar velocity constraints from five-band SZ effect measurements toward RX J1347.5-1145 with MUSIC and Bolocam from the CSO," *Astrophys. J.* **820**, 101 (2016).
20. A. Bracco et al., "Probing changes of dust properties along a chain of solar-type prestellar and protostellar cores in Taurus with NIKA," *Astron. Astrophys.* **604**, A52 (2017).
21. S. Steiger et al., "SCExAO/MEC and CHARIS discovery of a low-mass, 6 au separation companion to HIP 109427 using stochastic speckle discrimination and high-contrast spectroscopy," *Astron. J.* **162**(2), 44 (2021).
22. J. Golec, "Early high-resolution millimeter-wave maps from ToITEC," in *mm Univ. 2023 – Observ. the Univ. at mm Wavelengths, Eur. Phys. J. Web Conf.*, Vol. **293**, p. 00022 (2024).
23. R. Adam et al., "PITSZI: probing intra-cluster medium turbulence with Sunyaev–Zel'dovich imaging: application to the triple merging cluster MACS J0717.5+3745," *Astron. Astrophys.* **694**, A182 (2025).
24. A. Moullet et al., "Prima general observer science book," arXiv:2310.20572 (2023).
25. K. I. Öberg, R. Murray-Clay, and E. A. Bergin, "The effects of snowlines on C/O in planetary atmospheres," *Astrophys. J.* **743**(1), L16 (2011).
26. C. Eistrup, C. Walsh, and E. F. van Dishoeck, "Molecular abundances and C/O ratios in chemically evolving planet-forming disk midplanes," *Astron. Astrophys.* **613**, A14 (2018).
27. S. N. Raymond, T. Quinn, and J. I. Lunine, "Making other earths: dynamical simulations of terrestrial planet formation and water delivery," *Icarus* **168**, 1–17 (2004).
28. J. Blum and G. Wurm, "The growth mechanisms of macroscopic bodies in protoplanetary disks," *Annu. Rev. Astron. Astrophys.* **46**, 21–56 (2008).
29. C. Mordasini, Y. Alibert, and W. Benz, "Extrasolar planet population synthesis. I. Method, formation tracks, and mass-distance distribution," *Astron. Astrophys.* **501**, 1139–1160 (2009).
30. N. Madhusudhan, M. A. Amin, and G. M. Kennedy, "Toward chemical constraints on hot Jupiter migration," *Astrophys. J.* **794**(1), L12 (2014).
31. A. D. Schneider and B. Bitsch, "How drifting and evaporating pebbles shape giant planets. I. Heavy element content and atmospheric C/O," *Astron. Astrophys.* **654**, A71 (2021).

32. A. Kalyaan et al., "Linking outer disk pebble dynamics and gaps to inner disk water enrichment," *Astrophys. J.* **921**(1), 84 (2021).
33. B. Bitsch and J. Mah, "Enriching inner discs and giant planets with heavy elements," *Astron. Astrophys.* **679**, A11 (2023).
34. A. Houge, E. Macías, and S. Krijt, "Surviving the heat: multiwavelength analysis of V883 Ori reveals that dust aggregates survive the sublimation of their ice mantles," *Mon. Not. R. Astron. Soc.* **527**(4), 9668–9682 (2024).
35. C. J. Lada et al., "Spitzer observations of IC 348: the disk population at 2-3 million years," *AJ* **131**(3), 1574–1607 (2006).
36. M. Ansdell et al., "An ALMA survey of protoplanetary disks in the σ Orionis cluster," *Astron. J.* **153**, 240 (2017).
37. F. Long et al., "The First JWST view of a 30-Myr-old protoplanetary disk reveals a late-stage carbon-rich phase," arXiv:2412.05535 (2024).
38. K. M. Pontoppidan et al., "SuperDisks: a high-fidelity public database of protoplanetary and debris disk MIRI-MRS spectra," JWST Proposal. Cycle 4, ID. #7292 (2025).
39. C. Law, L. I. Cleeves, and DECO Team, "Early results from the disk-exoplanet C/Onnection (DECO) ALMA large program," in *Am. Astron. Soc. Meeting Abstr.*, Vol. 245, p. 206.04 (2025).
40. M. Vioque, "AGE-PRO: the ALMA survey of gas evolution in PROtoplanetary disks," in *EAS2024, Eur. Astron. Soc. Annu. Meeting* (2024).
41. A. E. Reines and M. Volonteri, "Relations between central black hole mass and total galaxy stellar mass in the local universe," *Astrophys. J.* **813**, 82 (2015).
42. S. J. Lilly et al., "Gas regulation of galaxies: the evolution of the cosmic specific star formation rate, the metallicity-mass-star-formation rate relation, and the stellar content of halos," *Astrophys. J.* **772**(2), 119 (2013).
43. R. Genzel et al., "Evidence for large-scale, rapid gas inflows in z 2 star-forming disks," *Astrophys. J.* **957**(1), 48 (2023).
44. P. Madau and M. Dickinson, "Cosmic star-formation history," *Annu. Rev. Astron. Astrophys.* **52**, 415–486 (2014).
45. R. C. Hickox and D. M. Alexander, "Obscured active galactic nuclei," *Annu. Rev. Astron. Astrophys.* **56**, 625–671 (2018).
46. P. D. Mitchell and J. Schaye, "How gas flows shape the stellar-halo mass relation in the EAGLE simulation," *Mon. Not. R. Astron. Soc.* **511**, 2948–2967 (2022).
47. D. Nelson et al., "First results from the TNG50 simulation: galactic outflows driven by supernovae and black hole feedback," *Mon. Not. R. Astron. Soc.* **490**, 3234–3261 (2019).
48. S. Veilleux et al., "Cool outflows in galaxies and their implications," *Aston. Astrophys. Rev.* **28**, 2 (2020).
49. M. Matsuura et al., "The global gas and dust budget of the Large Magellanic Cloud: AGB stars and supernovae, and the impact on the ISM evolution," *Mon. Not. R. Astron. Soc.* **396**, 918–934 (2009).
50. L. R. Nittler, "Presolar stardust in meteorites: recent advances and scientific frontiers," *Earth Planet. Sci. Lett.* **209**, 259–273 (2003).
51. M. L. Boyer et al., "The dust budget of the small magellanic cloud: are asymptotic giant branch stars the primary dust source at low metallicity?" *Astrophys. J.* **748**, 40 (2012).
52. M. Béthermin et al., "Confusion of extragalactic sources in the far-infrared: a baseline assessment of the performance of PRIMAger in intensity and polarization," *Astron. Astrophys.* **692**, A52 (2024).
53. J. M. S. Donnellan et al., "Overcoming confusion noise with hyperspectral imaging from PRIMAger," *Mon. Not. R. Astron. Soc.* **532**, 1966–1979 (2024).
54. M. Petach, M. Michaelian, and T. Nguyen, "Modifications to the MIRI cryocooler design to provide significant lift in the 2K to 4K range," *Mater. Sci. and Eng. Conf. Ser.* **755**, 012018 (2020).
55. A. Poglitsch et al., "The Photodetector Array Camera and Spectrometer (PACS) on the Herschel Space Observatory," *Astron. Astrophys.* **518**, L2 (2010).
56. J. M. Rodgers, J. P. McGuire, and R. J. Calvet, "Optical and opto-mechanical design of the PRIMA telescope," *Proc. SPIE* **12676**, 126760B (2023).
57. J. M. Rodgers et al., "Optical and opto-mechanical design of spectrometers for PRIMA," *Proc. SPIE* **12676**, 126760C (2023).
58. O. Krause et al., "The cold focal plane chopper of HERSCHEL's PACS instrument," *Proc. SPIE* **6273**, 627325 (2006).
59. W. Chen et al., "PRIMA space telescope cryocooling system," *Proc. SPIE* **12687**, 1268705 (2023).
60. W. Chen et al., "Effects of working fluid on performance of 4.5 k JT cooler," *IOP Conf. Ser.: Mater. Sci. Eng.* **1301**, 012017 (2024).
61. R. G. Ross, "Conceptual design and development history of the MIRI cryocooler system on JWST," *Cryocooler* **22**(1), 1 (2022).

62. P. J. Shirron et al., "Design and on-orbit operation of the soft X-ray spectrometer adiabatic demagnetization refrigerator on the Hitomi observatory," *J. Astron. Telesc. Instrum. Syst.* **4**(2), 021403 (2018).
63. A. M. Anderson et al., "Development and validation of a cryogenic far-infrared diffraction grating spectrometer used to post-disperse the output from a Fourier transform spectrometer," *Rev. Sci. Instrum.* **95**, 015116 (2024).
64. M. Buchan, "Development of a cryogenic far-infrared post-dispersed polarizing fourier-transform spectrometer," Master's thesis, University of Lethbridge (2024).
65. A. Cournoyer et al., "Design of a novel cryogenic stiffness-compensated reactionless scan mechanism for the Fourier transform spectrometer of SPICA SAFARI instrument," *Proc. SPIE* **11453**, 1145338 (2020).
66. A. Cournoyer et al., "Cryogenic testing towards TRL-5 demonstration of a novel stiffness-compensated, reactionless scan mechanism for the Fourier transform spectrometer of SPICA SAFARI instrument," *Proc. SPIE* **12190**, 121902E (2022).
67. P. Ade et al., "A review of metal mesh filters," *Proc. SPIE* **6275**, 62750U (2006).
68. M. J. Griffin et al., "The Herschel-SPIRE instrument and its in-flight performance," *Astron. Astrophys.* **518**, L3 (2010).
69. A. V. Sergeev, V. V. Mitin, and B. S. Karasik, "Ultrasensitive hot-electron kinetic-inductance detectors operating well below the superconducting transition," *Appl. Phys. Lett.* **80**(5), 817–819 (2002).
70. A. Andreev, "Thermal conductivity of the intermediate state of superconductors," *Zh. Eksperim. i Teor. Fiz.* **46** (1964).
71. J. Gao et al., "Noise properties of superconducting coplanar waveguide microwave resonators," *Appl. Phys. Lett.* **90**, 102507 (2007).
72. J. J. A. Baselmans et al., "Ultra-sensitive THz microwave kinetic inductance detectors for future space telescopes," *Astron. Astrophys.* **665**, A17 (2022).
73. K. Irwin and G. Hilton, *Transition-Edge Sensors*, pp. 63–150, Springer Berlin Heidelberg, Berlin, Heidelberg (2005).
74. R. J. Thornton et al., "The Atacama Cosmology Telescope: the polarization-sensitive ACTpol instrument," *Astrophys. J. Suppl. Ser.* **227**, 21 (2016).
75. P. A. R. Ade et al., "Bicep2. II. Experiment and three-year data set," *Astrophys. J.* **792**, 62 (2014).
76. J. T. Ward et al., "Mechanical designs and development of TES bolometer detector arrays for the Advanced ACTPol experiment," *Proc. SPIE* **9914**, 991437 (2016).
77. J. G. Staguhn et al., "The GISMO two-millimeter deep field in GOODS-N," *Astrophys. J.* **790**, 77 (2014).
78. D. A. Harper et al., "HAWC+, the far-infrared camera and polarimeter for sofia," *J. Astron. Instrum.* **07**(04), 1840008 (2018).
79. A. D. Beyer et al., "Ultra-sensitive transition-edge sensors for the Background Limited Infrared/Sub-mm Spectrograph (BLISS)," *J. Low Temp. Phys.* **167**, 182–187 (2012).
80. A. D. Beyer et al., "Effect of MO/CU superconducting bilayer geometry on ultra-sensitive transition-edge sensor performance," *IEEE Trans. Appl. Supercond.* **23**, 2100104 (2013).
81. A. D. Beyer et al., "Comparing transition-edge sensor response times in a modified contact scheme with different support beams," *J. Low Temp. Phys.* **176**, 299–303 (2014).
82. M. D. Audley et al., "Optical performance of an ultra-sensitive horn-coupled transition-edge-sensor bolometer with hemispherical backshort in the far infrared," *Rev. Sci. Instrum.* **87**, 043103 (2016).
83. M. L. Ridder et al., "Fabrication of low-noise tes arrays for the safari instrument on spica," *J. Low Temp. Phys.* **184**(1), 60–65 (2016).
84. P. Khosropanah et al., "Ultra-low noise tes bolometer arrays for safari instrument on spica," *Millimeter, Submillimeter, and Far-Infrared Detectors and Instrumentation for Astronomy VIII* **9914**, 99140B (2016).
85. T. Suzuki et al., "Development of ultra-low-noise TES bolometer arrays," *J. Low Temp. Phys.* **184**(1), 52–59 (2016).
86. M. Calvo et al., "The NIKA2 instrument, a dual-band kilopixel kid array for millimetric astronomy," *J. Low Temp. Phys.* **184**, 816–823 (2016).
87. I. Lowe et al., "Characterization, deployment, and in-flight performance of the BLAST-TNG cryogenic receiver," *Proc. SPIE* **11453**, 1145304 (2020).
88. S. Masi et al., "Kinetic inductance detectors for the OLIMPO experiment: in–flight operation and performance," *J. Cosmol. Astroparticle Phys.* **2019**(7), 003 (2019).
89. L. Foote et al., "Highly sensitive far-IR KIDs for PRIMA: optical characterization of a 25-micron array," *Proc. SPIE* **13102**, 131020D (2024).
90. L. Foote et al., "High-sensitivity kinetic inductance detector arrays for the PRobe far-infrared mission for astrophysics," *J. Low Temp. Phys.* **214**, 219–229 (2024).
91. S. Hailey-Dunsheath et al., "Characterization of a far-infrared kinetic inductance detector prototype for PRIMA," *IEEE Trans. Terahertz Sci. Technol.* (2025).

92. N. F. Cothard et al., "Monolithic silicon microlens arrays for far-infrared astrophysics," *Appl. Opt.* **63**, 1481 (2024).
93. C. D. Dowell, B. S. Hensley, and M. Sauvage, "Simulation of the far-infrared polarimetry approach envisioned for the PRIMA mission," arXiv:2404.17050 (2024).
94. S. J. C. Yates et al., "Demonstration of ultra-sensitive KIDs for future THz space borne polarimeters," arXiv:2501.03827 (2025).
95. K. K. Davis et al., "Complex field mapping of large direct detector focal plane arrays," *IEEE Trans. Terahertz Sci. Technol.* **9**, 67–77 (2019).
96. S. Gordon et al., "An open source, FPGA-based LeKID readout for BLAST-TNG: pre-flight results," *J. Astron. Instrum.* **05**, 1641003 (2016).
97. A. K. Sinclair et al., "CCAT-prime: RFSoC based readout for frequency multiplexed kinetic inductance detectors," *Proc. SPIE* **12190**, 121900W (2022).
98. D. Petrick et al., "Adapting the SpaceCube v2.0 data processing system for mission-unique application requirements," in *IEEE Aerosp. Conf.* (2015).
99. C. Wilson et al., "CSP hybrid space computing for STP-H5/ISEM on ISS," in *19th Annu. AIAA/USU Conf. Small Satell., SSC15-III-10* (2015).
100. C. Brewer et al., "NASA SpaceCube intelligent multi-purpose system for enabling remote sensing, communication, and navigation in mission architectures," in *34th Annu. AIAA/USU Conf. Small Satell., SSC20-VI-07* (2020).
101. S. Sabogal et al., "Spacecraft supercomputing experiment for STP-H6," in *31st Annu. AIAA/USU Conf. Small Satell., SSC17-XIII-02* (2017).
102. N. Perryman et al., "STP-H7-CASPR: a transition from mission concept to launch," in *35th Annu. AIAA/USU Conf. Small Satell., SSC21-WKII-08* (2021).
103. S. G. Kanekal et al., "The MERiT onboard the CeREs: a novel instrument to study energetic particles in the Earth's radiation belts," *J. Geophys. Res. (Sp. Phys.)* **124**, 5734–5760 (2019).
104. A. Geist et al., "NASA SpaceCube next-generation artificial-intelligence computing for STP-H9-SCENIC on ISS," in *37th Annu. AIAA/USU Conf. Small Satell., SSC23-P1-32* (2023).
105. R. Dubayah et al., "GEDI launches a new era of biomass inference from space," *Environ. Res. Lett.* **17**, 095001 (2022).
106. X. Sun et al., "Advanced silicon avalanche photodiodes on NASA's Global Ecosystem Dynamics Investigation (GEDI) mission," *Proc. SPIE* **11287**, 1128713 (2020).
107. W. A. Holmes et al., "Initial test results on bolometers for the Planck High Frequency Instrument," *Appl. Opt.* **47**, 5996–6008 (2008).

Biographies of the authors are not available.